JCB Journal of Cell Biology

ARTICLE

Hemicentin-mediated type IV collagen assembly strengthens juxtaposed basement membrane linkage

Claire A. Gianakas[1,2], Daniel P. Keeley[1], William Ramos-Lewis[1], Kieop Park[1], Ranjay Jayadev[1], Isabel W. Kenny[1], Qiuyi Chi[1], and David R. Sherwood[1,2]

Basement membrane (BM) matrices surround and separate most tissues. However, through poorly understood mechanisms, BMs of adjacent tissue can also stably link to support organ structure and function. Using endogenous knock-in fluorescent proteins, conditional RNAi, optogenetics, and quantitative live imaging, we identified extracellular matrix proteins mediating a BM linkage (B-LINK) between the uterine utse and epidermal seam cell BMs in *Caenorhabditis elegans* that supports the uterus during egg-laying. We found that hemicentin is secreted by the utse and promotes fibulin-1 assembly to jointly initiate the B-LINK. During egg-laying, however, both proteins' levels decline and are not required for B-LINK maintenance. Instead, we discovered that hemicentin recruits ADAMTS9/20, which facilitates the assembly of high levels of type IV collagen that sustains the B-LINK during the mechanically active egg-laying period. This work reveals mechanisms underlying BM–BM linkage maturation and identifies a crucial function for hemicentin and fibulin-1 in initiating attachment and type IV collagen in strengthening this specialized form of tissue linkage.

Introduction

Basement membranes (BMs) are thin, dense sheets of extracellular matrix that surround most tissues and provide structural and signaling support (Jayadev and Sherwood, 2017). Two of the most abundant core BM components are laminin and type IV collagen, which form independent self-oligomerizing networks. Laminin initiates BM formation and associates with cells by binding to integrin and dystroglycan receptors (Li et al., 2017). Type IV collagen networks have high tensile strength and allow BMs to mechanically support tissues (Fidler et al., 2018). BMs contain other core components such as perlecan, agrin, and nidogen that connect the collagen and laminin networks (Hohenester and Yurchenco, 2013) and harbor matricellular proteins, proteases, and growth factors (Jayadev et al., 2022). BMs usually separate tissues, but in some instances, BMs of adjacent tissues stably link and connect tissues to structurally support organs and facilitate specialized functions. One of the best characterized instances is in the kidney, where epithelial podocytes and the vascular endothelium synthesize distinct BMs that fuse to form the glomerular BM, which filters blood (Abrahamson, 1985; Keeley and Sherwood, 2019). Stable BM–BM linkages occur between other tissues as well (Keeley and Sherwood, 2019), including the alveolar and capillary BMs in the lung that facilitate gas exchange (Vaccaro and Brody, 1981; Makanya et al., 2013), and the capillary endothelial and parenchymal BMs of brain astrocytes that help form the blood–brain barrier (Sixt et al., 2001; Obermeier et al., 2013). Despite the importance of BM–BM attachments in stably joining tissues, little is known about how these connections are made and maintained because of the complexity of BMs, the difficulty of examining tissue interactions, and the lack of in vivo models that allow visualization and perturbation of BM components.

Caenorhabditis elegans is a powerful experimental model to understand how tissues attach through BM–BM linkages. *C. elegans* are optically transparent, have simple tissues, and BM components can be selectively targeted through conditional RNAi knockdown to determine time of function. Also, nearly all BM components have been endogenously tagged with genetically encoded fluorophores, which allows for visualization and quantitative analysis of localization, levels, and dynamics (Keeley et al., 2020). We previously characterized a transient BM–BM linkage between the gonadal and vulval BMs beneath the *C. elegans* anchor cell, which we termed a B-LINK (for BM linkage; Morrissey et al., 2014). B-LINK formation allows the anchor cell to invade through and degrade both BMs simultaneously to initiate uterine–vulval tissue connection (Sherwood and Sternberg, 2003; Hagedorn et al., 2013). The extracellular matrix protein hemicentin (*C. elegans* HIM-4) is secreted by the anchor cell just prior to invasion and forms punctae that reside

[1]Department of Biology, Duke University, Durham, NC; [2]Department of Pharmacology and Cancer Biology, Duke University, Durham, NC.

Correspondence to David R. Sherwood: david.sherwood@duke.edu.

© 2022 Gianakas et al. This article is distributed under the terms of an Attribution–Noncommercial–Share Alike–No Mirror Sites license for the first six months after the publication date (see http://www.rupress.org/terms/). After six months it is available under a Creative Commons License (Attribution–Noncommercial–Share Alike 4.0 International license, as described at https://creativecommons.org/licenses/by-nc-sa/4.0/).

between the BMs to promote their connection (Morrissey et al., 2014). The integrin heterodimer (αINA-1/βPAT-3) organizes hemicentin into punctae and the plakin cytolinker (VAB-10A) tethers the anchor cell to hemicentin (Morrissey et al., 2014). Suggesting a common role in BM–BM linkage, zebrafish hemicentins facilitate transient BM–BM connections during development between epithelia in fin epidermis and between somites and epidermis (Carney et al., 2010; Feitosa et al., 2012).

Most BM–BM linkages in vertebrates are stable, present in mechanically active tissues, and subject to stresses from blood flow and muscle contractions (Keeley and Sherwood, 2019). It is unclear whether these long-term BM–BM linkages require additional stabilizing matrix components. Along with the anchor cell B-LINK, we also identified a long-term B-LINK between the *C. elegans* uterine utse cell and epidermal seam cells that connects the uterus to the epidermis for the lifetime of the animal (Morrissey et al., 2014) and is thought to help the uterus withstand egg-laying mechanical stress (Newman et al., 1996; Schindler and Sherwood, 2013). All anchor cell B-LINK components localize to the utse–seam B-LINK, and their loss results in uterine prolapse after egg-laying begins, suggesting they are also required for this long-term BM–BM linkage (Morrissey et al., 2014; Vogel and Hedgecock, 2001). The matricellular protein fibulin-1 (FBL-1) also localizes to the utse–seam B-LINK, but its role in BM–BM linkage has not been examined (Muriel et al., 2005). Whether additional BM matrix components might contribute to this long-term B-LINK that supports a mechanically active tissue is not known.

Using endogenous fluorophore knock-in strains for hemicentin, α-integrin, and plakin, we found that the utse–seam B-LINK forms during the L4 larval stage, just prior to adulthood and egg-laying. Optogenetic inducible muscle contraction and RNAi-mediated knockdown revealed that hemicentin is required for the uterus to resist the physical stress of muscle contraction and egg-laying, providing direct evidence that the B-LINK anchors the uterus during egg passage. Through visual and RNAi screening, we discovered that the matrix proteins fibulin-1, perlecan (UNC-52), and type IV collagen (EMB-9) are also components of the utse–seam B-LINK. Conditional and tissue-specific RNAi knockdown revealed that hemicentin is secreted by the utse and promotes the assembly of fibulin-1, type IV collagen, and perlecan. A focused genome-wide RNAi screen revealed that hemicentin also recruits ADAMTS9/20 (GON-1), which is necessary for proper assembly of type IV collagen at the B-LINK. Quantitative imaging revealed that fibulin-1 and hemicentin reach peak levels at the B-LINK at the onset of egg-laying, and their loss causes early defects in utse–seam cell attachment, while later RNAi targeting does not affect the B-LINK. In contrast, type IV collagen and perlecan reach maximal levels later, during peak egg-laying, and type IV collagen loss only perturbs the B-LINK after egg-laying begins, suggesting that it helps resist the high mechanical stress of egg-laying. These findings identify matrix components required for a stable BM–BM linkage that resists mechanical stress and uncover distinct roles in mediating the initial formation and maintenance of a stable BM–BM connection.

Results

The utse and seam cells are connected by a B-LINK during the L4 larval stage

The utse–seam BM–BM interface forms a BM–BM linkage, which we have termed a B-LINK (Fig. 1, A–C; Morrissey et al., 2014; Vogel and Hedgecock, 2001). A key component of the B-LINK is hemicentin (*C. elegans* HIM-4), a large (5198-residue) conserved matrix protein that localizes to the utse–seam interface (Fig. 1 C and Video 1). The utse–seam B-LINK is also composed of the transmembrane integrin heterodimeric receptor (αINA-1/βPAT-3) and the cytosolic cytolinker plakin (VAB-10A; Morrissey et al., 2014; Fig. 1 C), and is thought to prevent uterine prolapse during egg-laying. The utse cell forms from fusion of uterine cells that contact the seam cells during the early L4 larval stage (Ghosh and Sternberg, 2014). However, it is not known when the B-LINK first develops to connect these tissues. To determine when the utse–seam B-LINK forms and how it develops over time, we examined the region where the utse and seam cells touch (visualized with *cdh-3p::mCh::PH* and *scmp::GFP::CAAX*, respectively). We found the utse and seam are already in contact by the mid-L4 stage, with a contact length of ∼50 µm and the utse midsection length of ∼25 µm (Fig. 2, A and B). The length of utse–seam contact and the utse midsection extended in the late-L4 stage and by the young adult, the utse–seam contact length was ∼60 µm and the midsection was ∼45 µm long. Additionally, by the young adult stage, the end of each utse arm turned inwards away from the seam (Fig. 2 B).

To determine when the B-LINK forms to connect the utse and seam cells, we examined B-LINK component localization from the mid-L4 to the early adult stage using homozygous mNeonGreen (mNG) endogenous knock-in strains of hemicentin::mNG (HIM-4), α-integrin::mNG (INA-1), and plakin::mNG (VAB-10A; Gally et al., 2016; Keeley et al., 2020; Fig. 2 C). B-LINK components were not consistently detected at the B-LINK at the mid-L4 stage (hemicentin 5/10; integrin and plakin 0/10), but during the mid to late L4 assembled to form a nascent B-LINK. While the α-integrin INA-1 levels plateaued during the late L4, hemicentin and plakin continued to increase until the young adult stage (Fig. 2 D). Together, these results indicate that the B-LINK begins to form during the mid L4 and then extends in length and is further enriched in B-LINK components by the young adult stage.

Perlecan, fibulin-1, type IV collagen, and papilinS enrich at the utse–seam B-LINK

In addition to hemicentin, fibulin-1 (FBL-1) also localizes to the utse–seam B-LINK, but it is unknown if fibulin-1 or any other matrix components have functions at this linkage (Morrissey et al., 2014; Muriel et al., 2005, 2012; Feitosa et al., 2012). To determine whether other matrix components are concentrated at the utse–seam B-LINK, we examined nine endogenously tagged BM matrix components—the core BM components γ-laminin::mNG (LAM-2), α1-type IV collagen::mNG or ::mRuby2 (EMB-9), perlecan::mNG (UNC-52), nidogen::mNG (NID-1), agrin::mNG (AGR-1), and type XVIII collagen::mNG (CLE-1), as well as the matricellular components papilinS::mNG (MIG-6S), papilinL::mNG (MIG-6L), spondin::mNG (SPON-1),

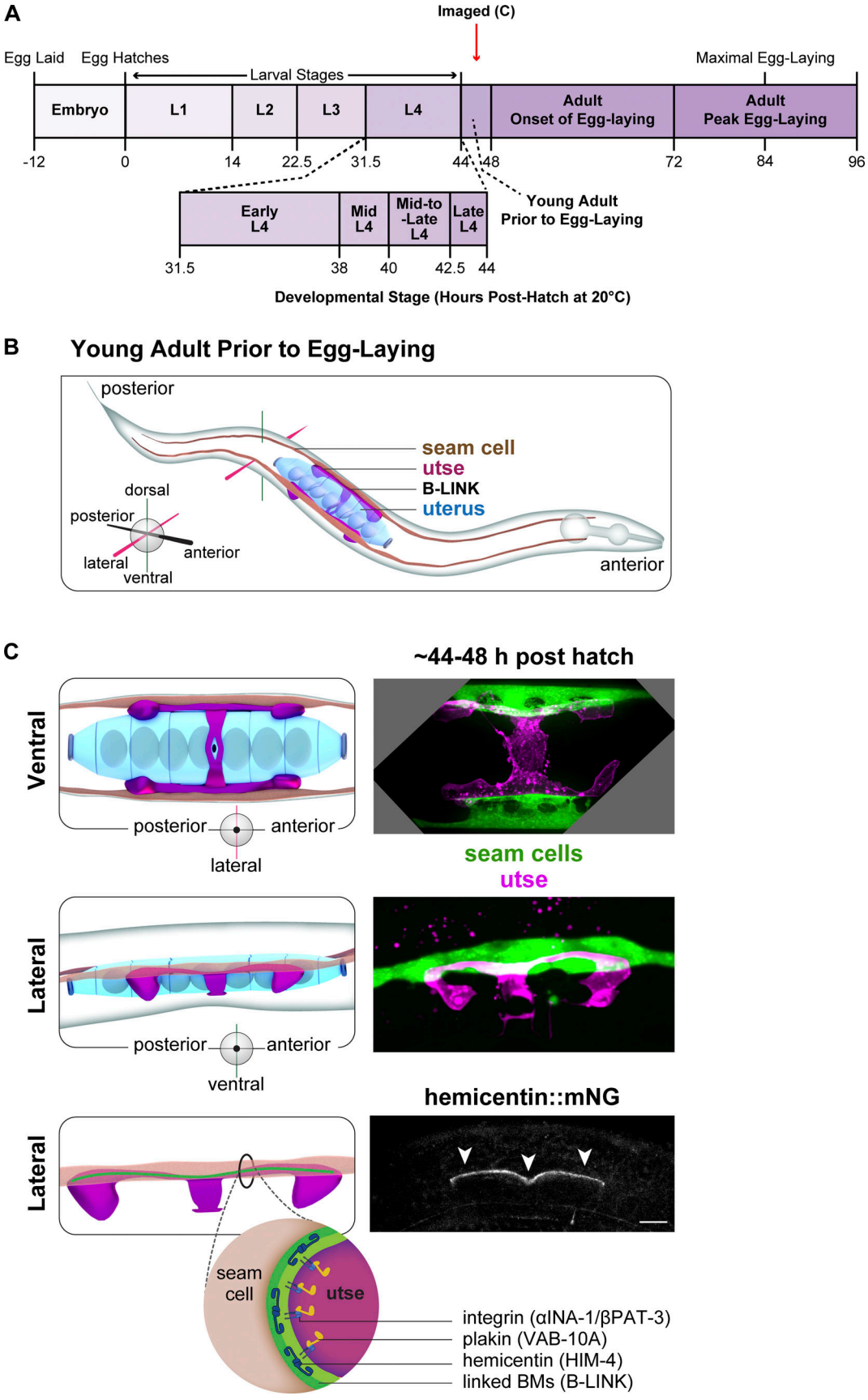

Figure 1. **A B-LINK joins the uterine utse cell and epidermal seam cells in *C. elegans*. (A)** A timeline of *C. elegans* development in h post-hatch showing developmental stages through peak egg-laying in adulthood. **(B)** A schematic of the utse–seam B-LINK in the young adult, just prior to egg-laying. At this time, a

B-LINK connects the utse (magenta) to the epidermal seam cells (brown), which run along the sides of the animal (individual seam cells not shown). The utse underlies the uterus (blue). **(C)** The utse (visualized with *cdh-3p::mCh::PH*, magenta) and seam cells (*scmp::GFP::CAAX*, green) from (top) a ventral perspective and (middle) a lateral perspective. The known B-LINK matrix component hemicentin (*C. elegans* HIM-4) visualized from a lateral perspective (bottom; arrowheads indicate B-LINK localization) sits between the utse BM and seam cell BM. Integrin (αINA-1/βPAT-3) and plakin (VAB-10A) are also components of the B-LINK (schematic) and function in the utse. Scale bar, 10 µm.

and mNG::fibulin-1 (FBL-1) (Jayadev et al., 2019; Keeley et al., 2020). *C. elegans* synthesizes two laminin heterotrimers with one of two α-chains, one β-chain, and one γ-chain, and a single triple helical type IV collagen molecule with two α1 chains and one α2 chain (Kramer, 2005). For simplicity, we refer to the levels and the presence of LAM-2 as laminin and α1-type IV collagen::mNG or ::mRuby2 (EMB-9) as type IV collagen. We performed a visual screen at the young adult stage to determine whether these matrix proteins are enriched at the utse–seam B-LINK in comparison with the neighboring unlinked gonadal BM (Fig. 3, A–C). As the B-LINK is a connection between two BMs, we defined enrichment as an over twofold higher fluorescence intensity compared to the single gonadal BM (where the utse resides). We found that perlecan, fibulin-1, and type IV collagen were significantly enriched over the gonadal BM (fold enrichment of 13.1, 8.7, and 4.7, respectively). PapilinS was also slightly enriched, although to a much lesser degree (~2.5 fold, Fig. 3, A–C). Together, this suggests that additional matrix components enrich at the utse–seam B-LINK and could have roles in BM–BM linkage.

B-LINK matrix components resist mechanical forces during egg-laying

The neural circuit that controls egg-laying is established during the L4 stage, and vulval muscle calcium transients suggest that muscle activity may generate forces on the B-LINK at this time (Ravi et al., 2018). However, it is not until the young adult stage (~48 h post-hatch) that neuronal signals trigger regular intervals of egg-laying muscle contractions followed by egg expulsion from the uterus (Schafer, 2006). Loss of hemicentin or other B-LINK components can result in utse–seam B-LINK failure after egg-laying begins, causing the rupture (Rup) phenotype where the worm's internal organs extrude through the vulva (Morrissey et al., 2014; Vogel and Hedgecock, 2001). However, whether egg-laying and muscle contractions are directly responsible for the Rup phenotype have not been determined. To test this, we used a strain with optogenetically inducible muscle contraction, achieved through expression of the ultraviolet light receptor LITE-1 in body wall and egg-laying muscles (Edwards et al., 2008). Expression of LITE-1 is thought to increase calcium levels and trigger muscle contraction (Edwards et al., 2008). We placed this strain on hemicentin RNAi at the L1 stage (immediately post-hatch) and exposed worms to blue light after 60 h (soon after egg-laying onset) to induce powerful, extended muscle contraction, and subsequent egg-laying. We found that light-induced muscle contraction caused the Rup phenotype in 76% of RNAi-treated animals (n = 68/90) compared to 3% of controls (n = 3/90; Fig. 3, D and E; and Videos 2 and 3; RNAi knockdown Table S2). These observations indicate that the utse–seam B-LINK helps the reproductive tissues resist the high mechanical stress of muscle contractions and egg-laying.

We next wanted to determine whether other BM components, particularly those enriched at the B-LINK, are functionally required for BM–BM linkage. To test this, we used mutants and RNAi knockdown to assess whether BM component loss resulted in the Rup phenotype (Table S1). RNAi feeding was started at the L1 stage (immediately post-hatch), and animals were observed each day for the Rup phenotype until 120 h post-hatch (past egg-laying peak). Loss of type IV collagen, papilinS, and fibuilin-1, which were identified in the visual screen, as well as laminin, caused rupture. Notably, the frequency of rupture upon loss of fibulin-1 was low, likely as fibulin-1 loss sharply reduces fertility and thus egg-laying (Muriel et al., 2005; Hesselson et al., 2004). Additionally, depletion of perlecan, which was also identified in the visual screen, did not cause rupture. This is likely due to the RNAi causing full muscle paralysis as perlecan helps anchor muscle attachments (Rogalski et al., 1995).

As type IV collagen, papilinS, and laminin are present in most *C. elegans* BMs, their loss might cause general BM defects that could lead to rupture (Gordon et al., 2019; Kawano et al., 2009; Keeley et al., 2020). To test whether the Rup phenotype for these components was the result of a B-LINK–specific defect, we initiated RNAi knockdown at the L3 stage, ~10 h before the development of the B-LINK (~30 h post-hatch). We reasoned that this late larval RNAi should reduce the later assembly of matrix components at the B-LINK but minimize depletion of components in the already assembled gonadal and seam cell BMs. RNAi against hemicentin, which specifically localizes to the B-LINK and is present at low or undetectable levels in the gonadal and seam cell BMs, was used as a positive control. L3-initiated loss of hemicentin and type IV collagen produced a robust Rup phenotype (Table S1). Importantly, L3 initiated RNAi significantly decreased hemicentin and type IV collagen levels at the B-LINK (~100 and 85%, respectively; Table S3), but type IV collagen gonadal BM levels were only slightly reduced (~30%; Table S3), strongly suggesting the Rup phenotype for these components is due to a B-LINK role. In contrast, L3 RNAi-mediated loss of laminin and papilin did not cause rupture, suggesting that the L1 RNAi Rup phenotype resulted from defects in BM and not a B-LINK role. Consistent with this, loss of laminin and papilinS causes dramatic perturbations in gonadal BM assembly (Keeley et al., 2020; Jayadev et al., 2019).

To further test whether type IV collagen and fibulin-1 are functionally required for the B-LINK, we completed optogenetic experiments on animals treated with type IV collagen or fibulin-1 RNAi and found that light-induced muscle contraction and egg-laying led to the Rup phenotype in both conditions (control RNAi, 2% rupture, n = 2/90; type IV collagen RNAi, 92% rupture, n = 85/92; fibulin-1 RNAi, 26% rupture, n = 23/90). We conclude that hemicentin, type IV collagen, and fibulin-1 (and

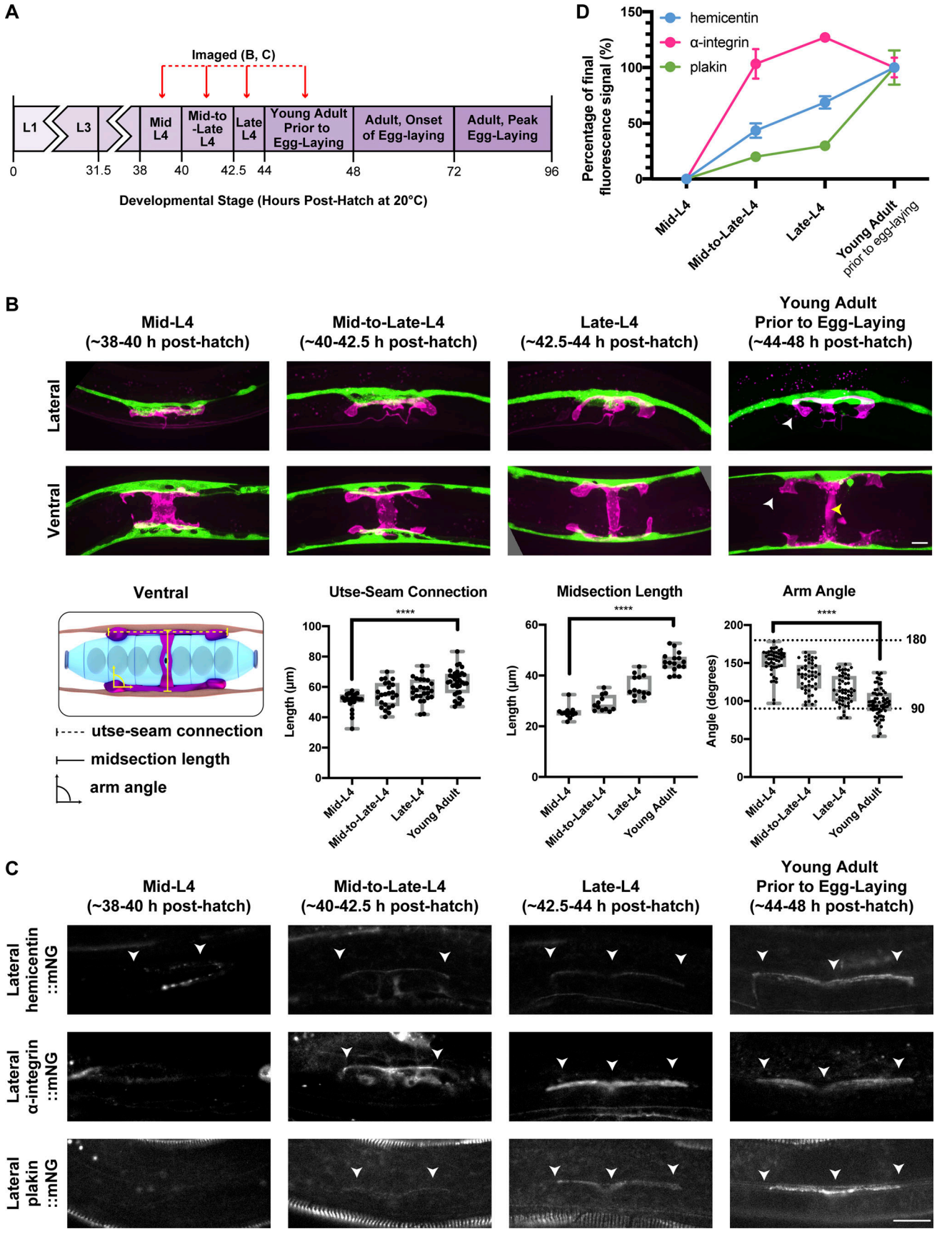

Figure 2. **Utse and seam cell association and B-LINK formation occur during the L4 larval stage. (A)** A schematic detailing the timing of imaging. **(B)** Top: Merged fluorescence images of the utse (magenta) and seam cells (green) viewed from a lateral and ventral perspective from the mid-L4 to the young adult

stage. By the young adult stage, the end of each utse arm has turned inwards away from the seam (white arrowheads) and the utse midsection is fully extended (yellow arrowhead). Bottom left: A schematic showing where measurements were taken. Bottom right: Mean length of utse–seam connection (n = 10 each), mean utse midsection length (n = 10 each), and mean angle between the turned in utse arm and the seam (n = 40 each). ****P < 0.0001, one-way ANOVA followed by post hoc Tukey's test. Box edges in boxplots depict the 25th and 75th percentiles, the line in the box indicates the median value, and whiskers mark the minimum and maximum values. **(C)** Localization of known B-LINK components (white arrowheads) viewed laterally from the mid-L4 to the young adult stage. Hemicentin images are also shown in Fig. 4 B. **(D)** Quantification of mean florescence intensity of each component at each timepoint as a percentage of the final mean fluorescence intensity of that component at the young adult stage. Error bars represent SEM (n = 10 all stages). Scale bars, 10 µm.

possibly perlecan) are components of the utse–seam B-LINK and are functionally required to resist the physical stress of egg-laying.

Hemicentin and fibulin-1 reach maximal levels prior to type IV collagen and perlecan

To investigate the roles of matrix components in B-LINK formation and function, we first examined their appearance and levels throughout B-LINK development. We found that B-LINK matrix components are undetectable or only beginning to be deposited at the mid-L4 stage (fibulin-1 and perlecan, 10/10; hemicentin, 5/10; type IV collagen, 0/10; Fig. 4, A and B). Component levels increased through the late-L4, and there was a robust buildup by the young adult stage. Interestingly, while hemicentin and fibulin-1 reached their maximal levels at egg-laying onset, type IV collagen and perlecan continued to enrich into the time of peak egg-laying (Fig. 4, A and B). We also assessed these component levels at the anchor cell B-LINK and found hemicentin was the only one specifically enriched beneath the anchor cell (Fig. S1), indicating the utse–seam B-LINK has a more complex matrix composition. As these strains are endogenously tagged with the same mNG fluorophore, we next compared levels at the utse–seam B-LINK. In adult animals (~72–96 h post hatch, peak egg-laying), type IV collagen and perlecan levels were ~10-fold higher than hemicentin and ~threefold higher than fibulin-1 (Fig. 4 C). These findings suggest hemicentin and fibulin-1 might play an earlier role in B-LINK formation, while type IV collagen and perlecan may function later in stabilizing the B-LINK during adulthood when there is higher mechanical strain from egg-laying.

Type IV collagen and perlecan are highly stable at the B-LINK, while hemicentin and fibulin-1 are more dynamic

To gain further insight into the roles of different matrix proteins in BM–BM linkage, we assessed the stability of type IV collagen, perlecan, fibulin-1, and hemicentin at the B-LINK by performing FRAP at the young adult stage (see Materials and methods). After photobleaching, fibulin-1 and hemicentin recovered ~50% or more of their original fluorescence intensity after 30 min. In contrast, type IV collagen and perlecan exhibited negligible recovery (Fig. 5, A–D). We explored type IV collagen dynamics further and found that type IV collagen recovered only ~40% of its original fluorescence 6 h after photobleaching (Fig. 5 E). This suggests that type IV collagen and perlecan are scaffolding components that stably link the utse–seam BMs together throughout adulthood, while the more dynamic hemicentin and fibulin-1 may play distinct dynamic structural roles and possibly regulatory functions at the B-LINK.

The utse contributes hemicentin to the utse–seam B-LINK

Most *C. elegans* BM components are secreted from body wall muscle into the extracellular fluid and then assembled on different tissues (Clay and Sherwood, 2015). Interestingly, hemicentin is expressed by the utse (Morrissey et al., 2014; Vogel and Hedgecock, 2001), suggesting that hemicentin, and possibly other B-LINK matrix components, could be contributed locally. To test this, we performed L1 RNAi targeting hemicentin, type IV collagen, fibulin-1, and perlecan using a strain where only the uterine tissue is sensitized to RNAi and scored for the Rup phenotype. We found that only utse-specific loss of hemicentin caused rupture, indicating that the utse contributes hemicentin to support the utse–seam B-LINK (Table S4). We also tested whether the seam cell contributes B-LINK components, but seam cell–specific RNAi did not cause any ruptures (Table S4). We conclude that hemicentin is provided by the utse, while type IV collagen, fibulin-1, and perlecan are likely recruited from the extracellular fluid.

Hemicentin is required for assembly of other B-LINK matrix components

The local production of hemicentin at the B-LINK suggested it might have an organizational role. Consistent with this idea, hemicentin has previously been reported to promote fibulin-1 assembly (Muriel et al., 2005). To confirm hemicentin's role in fibulin-1 assembly and determine whether assembly of type IV collagen and perlecan might also depend on hemicentin, we examined their levels at the utse–seam B-LINK at the young adult stage (48 h post-hatch) after loss of hemicentin (L1-mediated RNAi, 100% knockdown; Table S2). Consistent with a crucial organizational role at the B-LINK, hemicentin was required for the robust assembly of type IV collagen, fibulin-1, and perlecan (Fig. 6). In addition, loss of each of these components caused a reciprocal increase in hemicentin, suggesting feedback between hemicentin and other B-LINK components (Fig. S2). Fibulin-1 loss caused minimal changes in other B-LINK components, while type IV collagen loss caused a modest reduction of fibulin-1, but a significant decrease in perlecan (Fig. S3). These experiments suggest that hemicentin plays a crucial role in the assembly of other B-LINK matrix components, and that there is feedback between hemicentin and other B-LINK components.

Hemicentin and fibulin-1 facilitate initial B-LINK formation and type IV collagen is required for maintenance during egg-laying

Peak levels of hemicentin and fibulin-1 occur earlier at the B-LINK than the later accumulation of type IV collagen and perlecan. To test whether this signifies temporal roles in B-LINK formation and maintenance, we knocked down each B-LINK component using L1 RNAi and imaged the utse and seam cells at

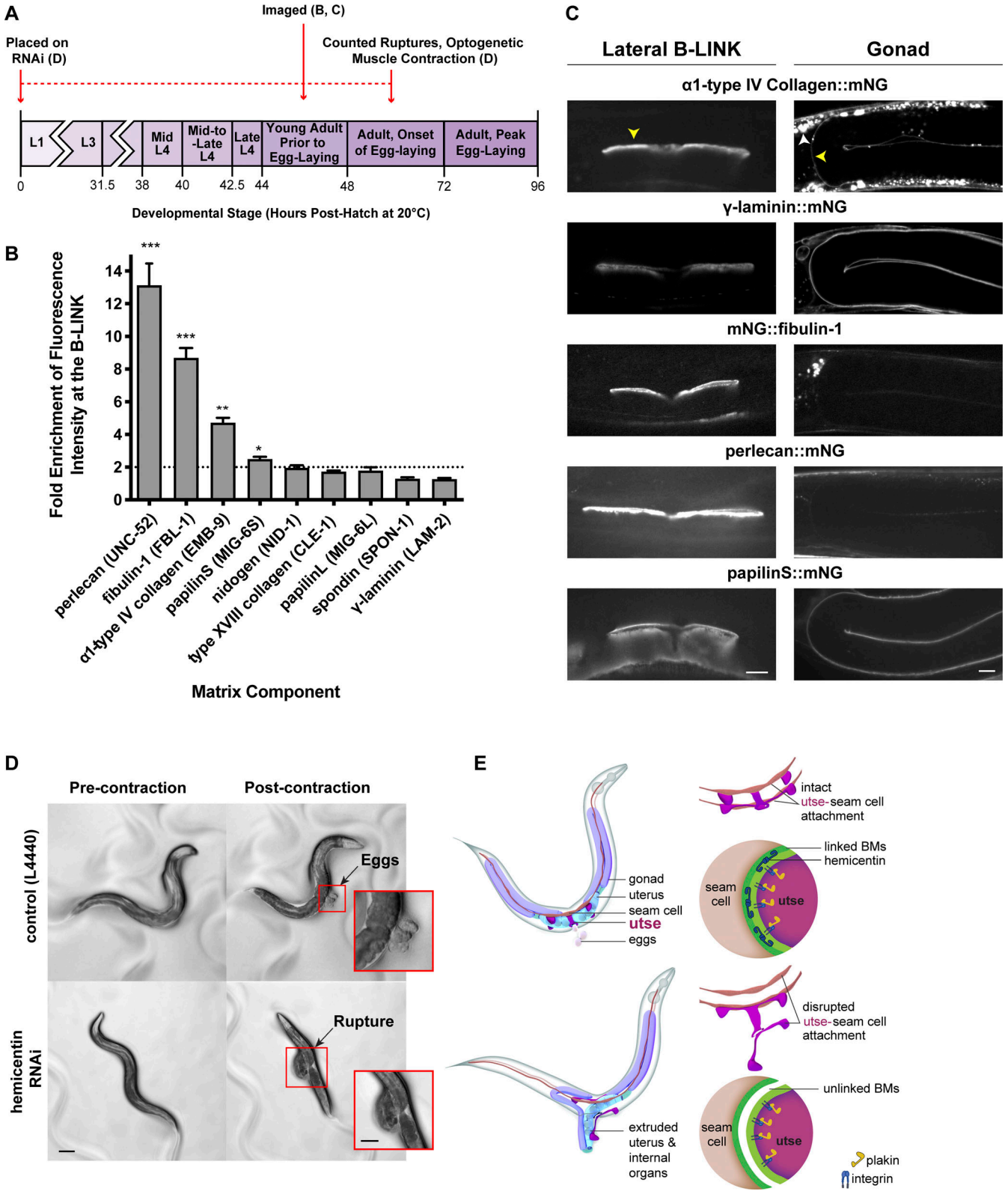

Figure 3. **Matrix enrichment at the B-LINK and the role of hemicentin in resisting egg-laying mechanical forces. (A)** A diagram showing the RNAi feeding and timing of optogenetic muscle contraction and imaging. **(B)** The quantification of fold enrichment of matrix component fluorescence intensity at the B-LINK compared to the gonadal BM at the young adult stage (n = 10 each). Agrin is not shown as it was undetectable at the B-LINK and in the gonadal BM (n = 10 each). ***P < 0.0001, **P < 0.001, *P < 0.01, unpaired two-tailed Student's t test comparing B-LINK signal to two times the gonad signal (to account for double BM at the B-LINK). Error bars represent SEM. **(C)** Fluorescence images of enriched matrix components and a representative non-enriched component (γ-laminin::mNG) at the young adult stage at the B-LINK and in the gonadal BM. Yellow arrowheads indicate location of fluorescence intensity measurements. White arrowhead indicates α1-type IV collagen localized in the muscle endoplasmic reticulum where it is assembled. **(D)** Transgenic worms expressing the

ultraviolet light receptor LITE-1 in body wall and egg-laying muscles (*lite-1*(*ce314*); *ceIs37* [*myo-3p::lite-1 + myo-3p::GFP*]) were plated on control (T444T empty vector) and hemicentin (*him-4*) RNAi and after 60 h were exposed to 488 nm light for 7 s to induce muscle contractions that forced egg-laying. Images show worms both pre- and post-contraction. Regions of the animals in the red box are magnified in the insert to show egg-lay and rupture (control rupture: 3%, *n* = 3/90; hemicentin RNAi knockdown rupture: 76%, *n* = 68/90). Images are stills from Videos 2 (control RNAi) and 3 (hemicentin RNAi). **(E)** A schematic model of utse–seam B-LINK rupture upon loss of hemicentin. Scale bars in C, 10 µm. Main scale bar in D, 100 µm; insert scale bar, 50 µm.

the mid-L4, late-L4, and adult onset of egg-laying stages (Table S2). Defects in the B-LINK were indicated by a lack of contact between the utse and seam cells (utse–seam gaps). Fibulin-1 loss caused the most penetrant early defect at the mid-L4 stage, indicating fibulin-1 has the earliest role at the utse–seam B-LINK (Fig. 7, A–C). Importantly, contact between the utse and seam at the early-L4 stage was unimpaired after fibulin-1 loss (10/10 animals), suggesting fibulin-1 loss does not alter the initial utse and seam cell contact. We found loss of hemicentin also caused an early B-LINK defect, with the utse occasionally pulling off from the seam at the mid L4, but more significantly by the late L4 (Fig. 7, B and C). Mirroring these temporal functions, fibulin-1 deposition was consistently present at the mid L4 (Fig. 4 B; 10/10 animals), while hemicentin was not (Fig. 4 B; 5/10 animals). Knockdown of hemicentin did not severely affect early fibulin-1 deposition (~20% fibulin-1 reduction, Fig. 7 D), although fibulin-1 became reliant on hemicentin by the late L4 (Fig. 7 D). These data indicate that fibulin-1 has an early hemicentin-independent role in mediating utse–seam B-LINK formation, but by the late L4 becomes dependent on hemicentin. Notably, the combined loss of hemicentin and fibulin through double RNAi treatment caused a B-LINK defect at the late L4 more severe than loss of either one alone, suggesting that hemicentin and fibulin have at least partially independent functions (Fig. 7, B and C). Loss of type IV collagen did not affect the utse–seam B-LINK through the L4 stage (Fig. 7, B and C), and only caused utse–seam separation in the adult at egg-laying onset (Fig. 7, B and C). These results strongly suggest that type IV collagen strengthens the B-LINK so that it can withstand higher mechanical forces during egg-laying. Perlecan RNAi did not cause utse–seam separation at any timepoint (Fig. 7, B and C), likely because its loss led to complete paralysis and the absence of mechanical stress on the B-LINK.

Hemicentin and fibulin-1 have early roles in B-LINK formation, but not maintenance

We next examined the role of hemicentin, fibulin-1, and type IV collagen during B-LINK maintenance. We first assessed hemicentin by initiating RNAi knockdown at the early-L4 (~5 h before B-LINK formation), the mid-L4 (the start of B-LINK formation), the mid-to-late-L4 (~5 h after B-LINK starts to form), or the young adult stage (~10 h after B-LINK starts to form) and scoring for the Rup phenotype (Fig. 8 A and Table S5). Knockdown of hemicentin at the early L4 or mid L4 (the start of B-LINK formation) caused rupture, while knockdown of hemicentin at the young adult stage did not cause rupture despite a complete loss of detectable hemicentin (Fig. 8 B and Table S5). This suggests hemicentin is required during the early stages of utse–seam B-LINK formation, but not for B-LINK maintenance. To confirm this, we placed animals on hemicentin RNAi at the young adult stage (48 h post-hatch, ~10 h after B-LINK initiation) and imaged the utse and seam cells 24 h later (72-h post-hatch, just before peak egg-laying). This later RNAi plating did not cause separation of the utse and seam cells, indicating there was no B-LINK defect (Fig. 8 C). These results provide compelling evidence that hemicentin has an early role during utse–seam B-LINK formation, but is dispensable after the B-LINK is established.

We next investigated fibulin-1. As fibulin-1 is required for fertility, which affects the penetrance of the Rup phenotype, we directly examined the utse and seam cells. To determine whether fibulin-1 was required after its early role in B-LINK formation, we placed animals on fibulin-1 RNAi at the young adult stage (~10 h after B-LINK initiation) to assess utse–seam separation 24 h later. RNAi platings at this stage, however, did not result in sufficient fibulin-1 protein knockdown (Table S6). Thus, RNAi was used to knockdown fibulin-1 at the mid-to-late-L4 stage and the utse and seam cells were examined 32 h later at the onset of egg-laying. Although RNAi knockdown of fibulin-1 was >50% (Table S6), fibulin-1 loss did not cause utse–seam separation (Fig. 8 D). In contrast, early loss of fibulin-1 (L1 RNAi, also ~50% knockdown; Table S2) resulted in separation of the utse and seam cells, indicating a B-LINK defect (Fig. 8 D). These results strongly suggest that like hemicentin, fibulin-1 has a specific early role in B-LINK formation, but not in maintenance during egg-laying.

As type IV collagen appeared to be required for maintenance of the mature B-LINK, we hypothesized that RNAi knockdown of type IV collagen beginning at the late-L4 and young adult stages would cause rupture during peak egg-laying. However, no significant ruptures were observed (late L4, 1/35; young adult, 1/246). We hypothesized that since type IV collagen is highly stable at the B-LINK, the lack of late ruptures could be because type IV collagen loss was not significant enough to disrupt the B-LINK. To test this, we knocked down type IV collagen using L1 RNAi and measured type IV collagen levels at the B-LINK at rupture onset (~72 h post hatch), thus determining the threshold collagen levels when the B-LINK begins to fail. We then compared this to type IV collagen levels after later RNAi platings (Fig. 8, E and F). Although L4 RNAi platings caused ~75% knockdown of type IV collagen (at least 60 h on RNAi; Fig. 8 E), the remaining type IV collagen levels were >twofold higher than type IV collagen levels when ruptures were first observed (Fig. 8 F). To allow more time for knockdown, we plated worms on type IV collagen RNAi at the young adult stage (48 h post-hatch) and scored for rupture through the adult decline in egg-laying stage (end of day 4 adult) and found that ruptures were significantly higher than controls at this later timepoint (control 2%, 2/90; type IV collagen RNAi 16%, 14/90; fisher's exact test $P < 0.01$). Together, this indicates that hemicentin and fibulin-1

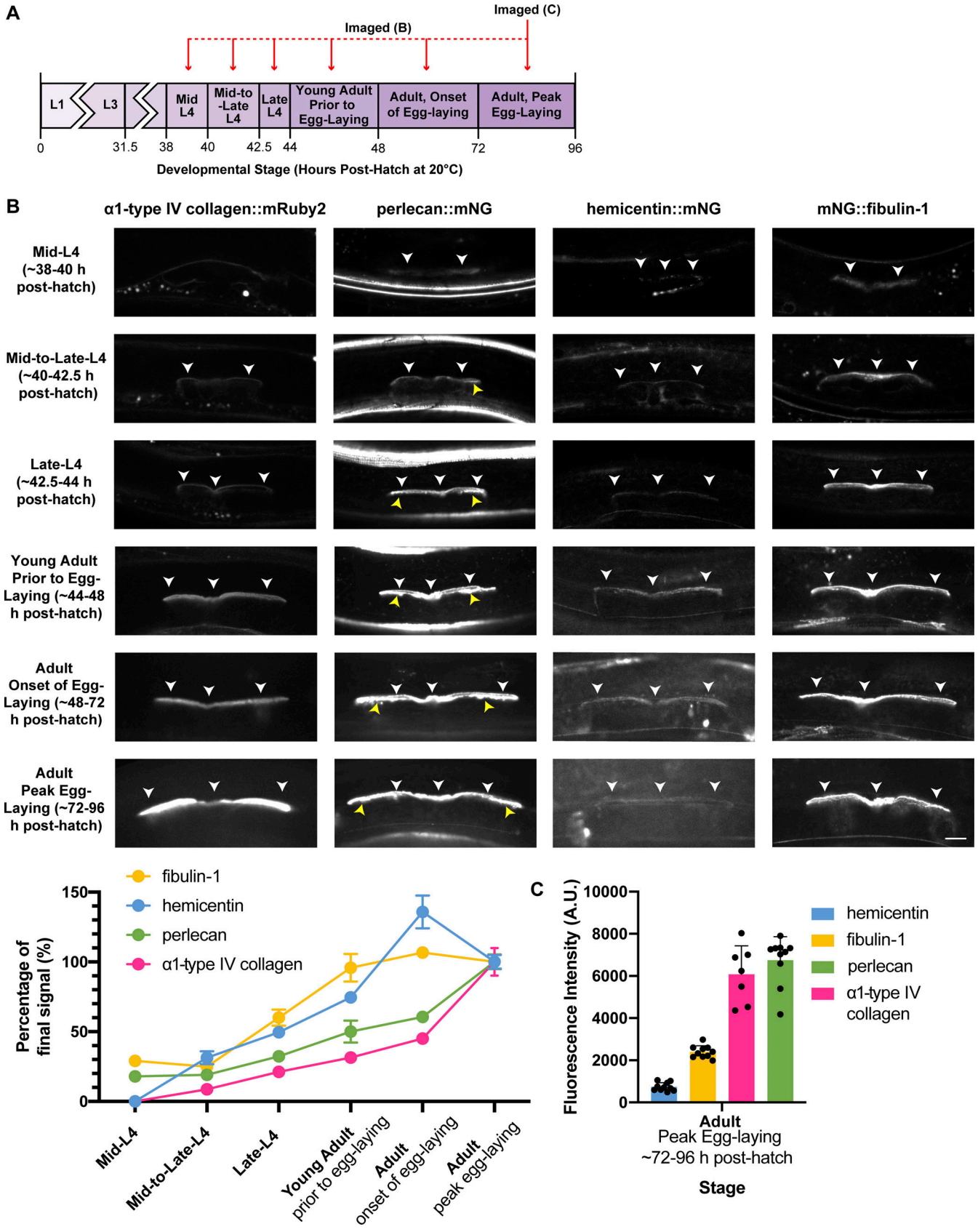

Figure 4. **B-LINK levels of hemicentin and fibulin-1 peak earlier than type IV collagen and perlecan. (A)** A schematic delineating the timing of imaging of utse–seam B-LINK matrix components in B. **(B)** Top: Fluorescence images of endogenous α1-type IV collagen::mRuby2, perlecan::mNG, hemicentin::mNG and mNG::fibulin-1 at the B-LINK (white arrowheads) from mid-L4 to peak egg-laying in the adult (n = 10 each). Yellow arrowheads indicate perlecan signal in the

vulval muscle attachment sites below the ends of the B-LINK. Mid-L4 through young adult hemicentin images are also shown in Fig. 2 C. Bottom: Quantification of mean florescence intensity of each B-LINK matrix component at each timepoint as a percentage of the final mean fluorescence intensity of that component in the peak egg-laying adult (n = 10 all stages). **(C)** Quantification of fluorescence intensity of all endogenously mNG tagged utse–seam B-LINK matrix components (imaged at the same exposure to compare levels). Error bars in graphs represent SEM. Scale bar, 10 µm.

initiate utse–seam BM–BM attachment, while type IV collagen is highly stable and functions to maintain the utse–seam B-LINK during the mechanically active time of egg-laying.

Hemicentin and fibulin-1 levels dramatically decline at the B-LINK during egg-laying

As our data showed early roles for fibulin-1 and hemicentin in mediating utse–seam B-LINK formation and later roles for type IV collagen and perlecan in B-LINK maintenance, we examined the localization of these components during B-LINK maintenance. We quantified component levels at the adult peak egg-laying stage (72 h post-hatch) as well as two later timepoints when egg-laying is gradually declining due to exhaustion of sperm and germline aging (120 h post-hatch/~day 3 adult and 168 h post-hatch/~day 4 adult; Fig. 9 A; Kocsisova et al., 2019). Both hemicentin and fibulin-1 levels significantly decreased throughout adulthood reaching low and, in the case of hemicentin, nearly undetectable levels (Fig. 9, B and C). In contrast, perlecan levels were maintained (n = 10 animals per stage) and type IV collagen increased (n = 10 per stage), consistent with a role in B-LINK maintenance (Fig. 9, B and C).

Hemicentin recruits type IV collagen through ADAMTS9/20

Given the critical role of type IV collagen in mediating B-LINK maintenance, we wanted to determine how hemicentin promotes collagen assembly. Hemicentin is not known to bind to type IV collagen (Zhang et al., 2021 *Preprint*), so we hypothesized that hemicentin might recruit another protein that mediates collagen assembly. We reasoned that loss of this protein would result in a similar phenotype to type IV collagen loss and thus compiled a list of 403 genes using Wormbase (see Materials and methods) whose RNAi knockdown or genetic loss leads to the Rup phenotype (Table S7). We focused on 52 genes encoding secreted or transmembrane proteins and removed genes not likely to be directly involved with collagen recruitment, such as metabolic transporters, cuticular collagens, and gap junction components. RNAi-mediated reduction of the remaining 11 genes revealed that loss of ADAMTS9/20 (GON-1) led to the strongest effect on type IV collagen levels—a >50% reduction at the B-LINK at egg-laying onset (Fig. 10, A and B; and Table S7). Importantly, ADAMTS9/20::mNG localized to the B-LINK at the time of type IV collagen recruitment, and its localization was dependent on hemicentin, but largely not on other BM components, with only a modest dependence on type IV collagen (Fig. S4 C and Fig. 10 C). Furthermore, loss of ADAMTS9/20 specifically affected collagen recruitment, but not the recruitment of other B-LINK components (Fig. S4 C). To examine how ADAMTS9/20 affects type IV collagen assembly, we used a strain with α1-type IV collagen::mRuby2 and performed FRAP experiments on control and ADAMTS9/20 RNAi-treated animals. Animals were plated on RNAi at the L2 stage as L1 RNAi made the animals prone to rupturing, which prevented long-term imaging. After photobleaching at the young adult stage (prior to egg-laying), type IV collagen recovered ~20% of its original fluorescence intensity after 2 h. In contrast, in animals where ADAMTS9/20 was reduced, type IV collagen recovered only ~9% (Fig. 10 D). We conclude that ADAMTS9/20 helps mediate hemicentin-dependent assembly of type IV collagen at the B-LINK.

Discussion

BMs enwrap and separate most tissues, allowing them to slide along each other (Brown, 2011). However, at specific locations, including the lung alveoli, kidney glomeruli, and astrocytes in the blood–brain barrier, adjacent tissues link their BMs to stabilize tissues and build specialized organs (Keeley and Sherwood, 2019). Due to the challenge of dissecting complex tissue interactions, the mechanisms that mediate BM–BM tissue attachment are poorly understood. We previously characterized a transient B-LINK that facilitates anchor cell invasion through linked uterine and vulval BMs and is composed of the matricellular matrix protein hemicentin, the matrix receptor integrin, and the cytolinker plakin (Morrissey et al., 2014). We also discovered that these proteins are part of a stable B-LINK that connects the multi-nucleated uterine utse cell to seam epidermal cells for the lifetime of the animal. This utse–seam BM–BM linkage has been proposed to maintain the uterus within the animal during egg-laying (Vogel and Hedgecock, 2001) but it was unknown if it contained additional matrix components to mediate a more robust BM–BM linkage, and whether it directly functioned to resist the high mechanical stress of egg-laying.

Using live imaging and endogenous mNG-tagged hemicentin, integrin, and plakin, we discovered that the B-LINK begins to form at the mid-L4 stage and enriches in B-LINK components by the young adult stage, just prior to egg-laying. Using LITE-1 optogenetic stimulation of body wall and egg-laying muscle contractions (Edwards et al., 2008) on hemicentin-depleted animals (weakened utse–seam B-LINK), we found that egg-laying causes uterine prolapse. These experiments establish that the utse–seam B-LINK forms prior to egg-laying and functions to resist mechanical forces associated with muscle contraction and egg-laying.

Through screening and timed RNAi depletion, we discovered the utse–seam B-LINK has additional matrix components not found at the anchor cell B-LINK including the matricellular protein fibulin-1, and core BM proteins type IV collagen and perlecan. Similar to hemicentin, loss of fibulin-1 and type IV collagen led to uterine prolapse. Perlecan loss, however, eliminated egg-laying muscle contractions due to its role in anchoring muscle attachments (Rogalski et al., 1995), thus impeding the determination of its functional role at the B-LINK. An important

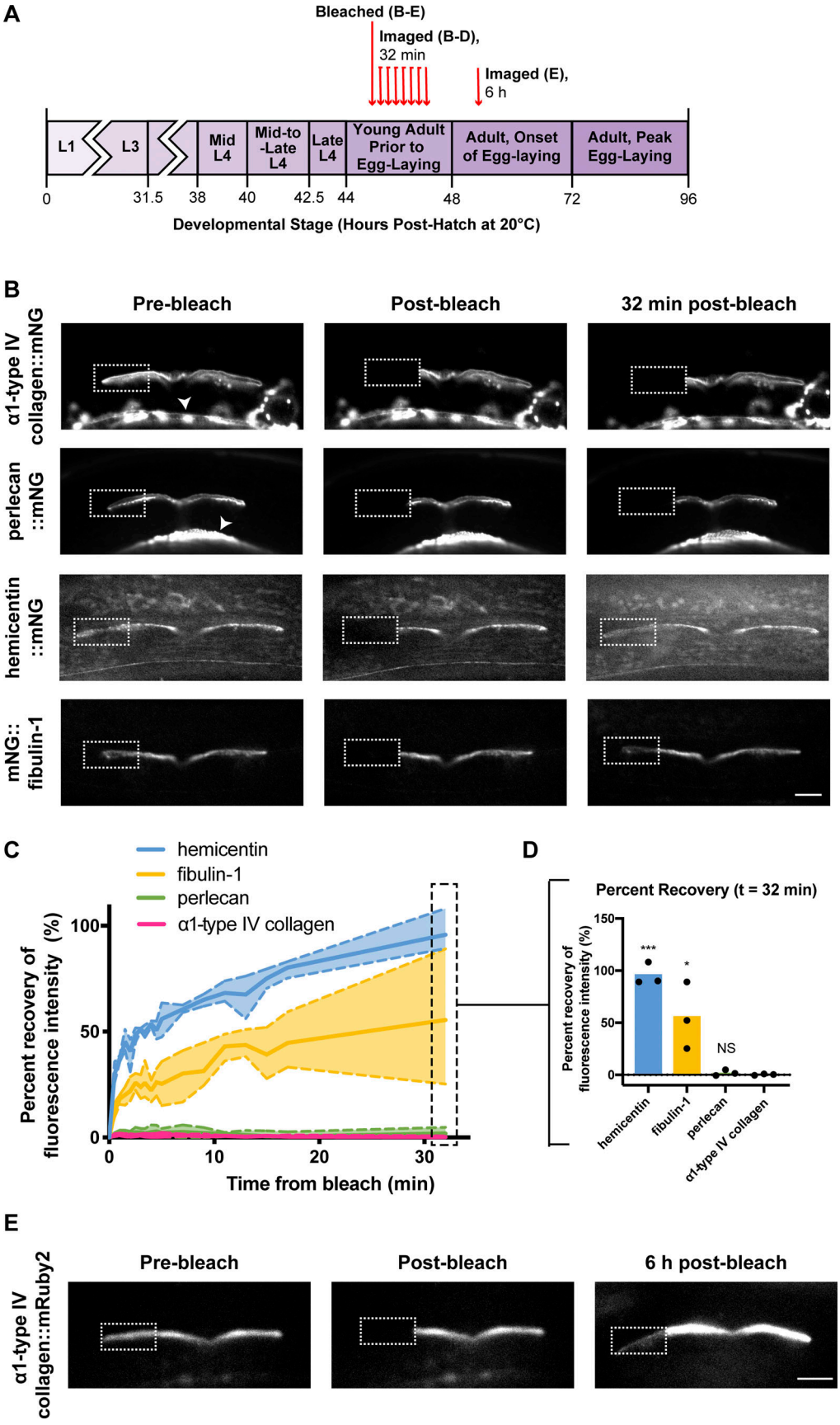

Figure 5. **Type IV collagen and perlecan are highly stable at the utse–seam B-LINK, hemicentin and fibulin-1 are dynamic. (A)** A schematic showing the timing of photobleaching and imaging. **(B)** Fluorescence images of α1-type IV collagen::mNG, perlecan::mNG, hemicentin::mNG, and mNG::fibulin-1 before

photobleaching, immediately after photobleaching, and 32 min post-photobleaching in young adult animals. Dotted white box indicates bleached region. White arrowheads indicate α1-type IV collagen::mNG and perlecan::mNG in the body wall muscle. **(C)** A line graph showing the fluorescence recovery of each component in the young adult B-LINK over 32 min (n = 3 each). Dashed lines represent the minimum and maximum values for each matrix component. **(D)** Bar graph shows the mean percent recovery of each component after 32 min. All components were compared with α1-type IV collagen. ***P < 0.001, *P < 0.01, one-way ANOVA followed by post hoc Dunnet's test. **(E)** Fluorescence images of α1-type IV collagen::mNG, before photobleaching, immediately after photobleaching, and 6 h post-photobleaching in adult animals (46 ± 10% recovery, n = 3). Dotted white box indicates bleached region. Scale bars, 10 µm.

strength of this in vivo model is the ability to perform timed RNAi knockdown through feeding, allowing determination of temporal roles for matrix proteins. Knockdown of the core BM components type IV collagen and laminin at the L1 stage dramatically disrupts the gonadal BM by the young adult stage (Jayadev et al., 2019; Gordon et al., 2019), which leads to the Rup phenotype due to disruption of the B-LINK's anchoring BM. By feeding worms at the L3 stage, we were able to specifically target the later deposition of collagen between the BMs at the B-LINK, and leave the gonadal BM intact, as evidenced by modest collagen reduction in the gonadal BM. This allowed us to establish a functional role for type IV collagen at the B-LINK and determine that laminin was not functionally required at the B-LINK, as L3 RNAi targeting of laminin did not cause uterine prolapse.

Similar to hemicentin, each newly identified B-LINK matrix component appeared at the B-LINK between the mid-L4 and the late-L4 stages and enriched into the young adult stage. We also discovered that hemicentin is contributed to the B-LINK locally from the utse and plays a key role in promoting the assembly of all other B-LINK matrix components as the B-LINK matures. Notably, previous transmission electron microscopy studies have observed electron dense extracellular matrix material localized between the utse and seam cell BMs that is lost in hemicentin null mutants (Vogel and Hedgecock, 2001). These observations are consistent with this material being composed of hemicentin and other B-LINK matrix components whose assembly hemicentin promotes. We also found that loss of fibulin-1, type IV collagen, and perlecan caused a reciprocal increase in hemicentin, suggesting feedback mechanisms set the precise levels of matrix proteins at the B-LINK. It will be interesting in future studies to determine the mechanisms of feedback and if they involve mechanical load. Close association of hemicentin with fibulins and collagens has been observed in both *C. elegans* and vertebrates (Feitosa et al., 2012; Lin et al., 2020; Muriel et al., 2005). The physical-binding partners of hemicentins, however, are poorly understood (Zhang et al., 2021 *Preprint*). Studies in *C. elegans* have shown that hemicentin promotes the assembly of fibuilin-1 at several extracellular sites and requires EGF repeats 4 and 5 of fibulin-1, suggestive of a direct interaction (Muriel et al., 2005, 2012). Our data indicate that hemicentin promotes type IV collagen assembly through ADAMTS9/20 (GON-1), as GON-1 B-LINK localization was dependent on hemicentin and its loss reduced type IV collagen assembly. The only identified substrates of ADAMTS9/20 in vertebrates are aggrecan and versican (Kelwick et al., 2015), which are not present in *C. elegans*. This suggests that GON-1 has another substrate(s) that promotes type IV collagen assembly. Although paradoxical that an ADAMTS protease promotes B-LINK type IV collagen incorporation, the matrix metalloproteinase MMP-1 is required for normal type IV collagen assembly in the BM of *Drosophila* embryos and larvae (Stevens and Page-McCaw, 2012; Matsubayashi et al., 2020). Proteolysis might facilitate type IV collagen incorporation into extracellular matrices. Finally, we found that perlecan assembly during B-LINK maturation was dependent on collagen. Perlecan binds type IV collagen (Hohenester and Yurchenco, 2013), suggesting hemicentin may promote perlecan enrichment indirectly through collagen.

Using timed RNAi depletion, photobleaching, and quantitative fluorescence analysis, we also determined distinct properties and temporal requirements for matrix components at the utse–seam B-LINK (summarized in Fig. 10 D). We found that hemicentin and fibulin-1 have dynamic associations, with recovery half-lives of <30 min, and reach peak levels prior to egg-laying. In contrast, perlecan and type IV collagen reach peak levels later during egg-laying. Consistent with their early deposition, hemicentin and fibulin-1 loss caused B-LINK disruption and utse–seam splitting at the mid- and late-L4 stages before type IV collagen levels ramped up. Although the B-LINK does not resist the mechanical forces of egg-laying at this time, vulval and possibly uterine muscle contractions appear to occur in the L4 stage (Ravi et al., 2018), which would place mechanical stress on the B-LINK. Notably, once type IV collagen began to build up during egg-laying, hemicentin and fibulin-1 were no longer required to maintain the B-LINK, and their endogenous levels dramatically decreased. This supports the idea of a specific early role for fibulin-1 and hemicentin in mediating the initial stages of BM–BM linkage. It is likely that hemicentin and fibulin-1 have independent functions in linking the BMs, as loss of fibulin-1 led to defects prior to loss of hemicentin and the combined loss of hemicentin and fibulin-1 led to a greater defect in BM–BM linkage than loss of either alone. Consistent with the notion of independent functions, hemicentin alone promotes BM–BM linkage under the anchor cell (Morrissey et al., 2014), and hemicentin-1 in zebrafish mediates fin fold BM–BM linkage (Carney et al., 2010). Notably, hemicentin-2 and fibulin-1 also function together in zebrafish to facilitate a transient somite and epithelial BM–BM connection (Feitosa et al., 2012). These observations suggest that hemicentin and fibulin-1 function as a dynamic specialized matrix, each with separate and perhaps some redundant functions that can rapidly assemble to stabilize BM–BM linkages, withstand modest mechanical forces, and help promote the assembly of a more stable BM–BM tethering matrix.

In contrast to hemicentin and fibulin-1, we found that type IV collagen and perlecan are highly stable at the utse–seam B-LINK and enrich to maximal levels after egg-laying onset. Consistent with this later buildup, type IV collagen depletion only caused utse–seam B-LINK defects at egg-laying onset, suggesting it functions to bear high mechanical loads. Supporting this idea,

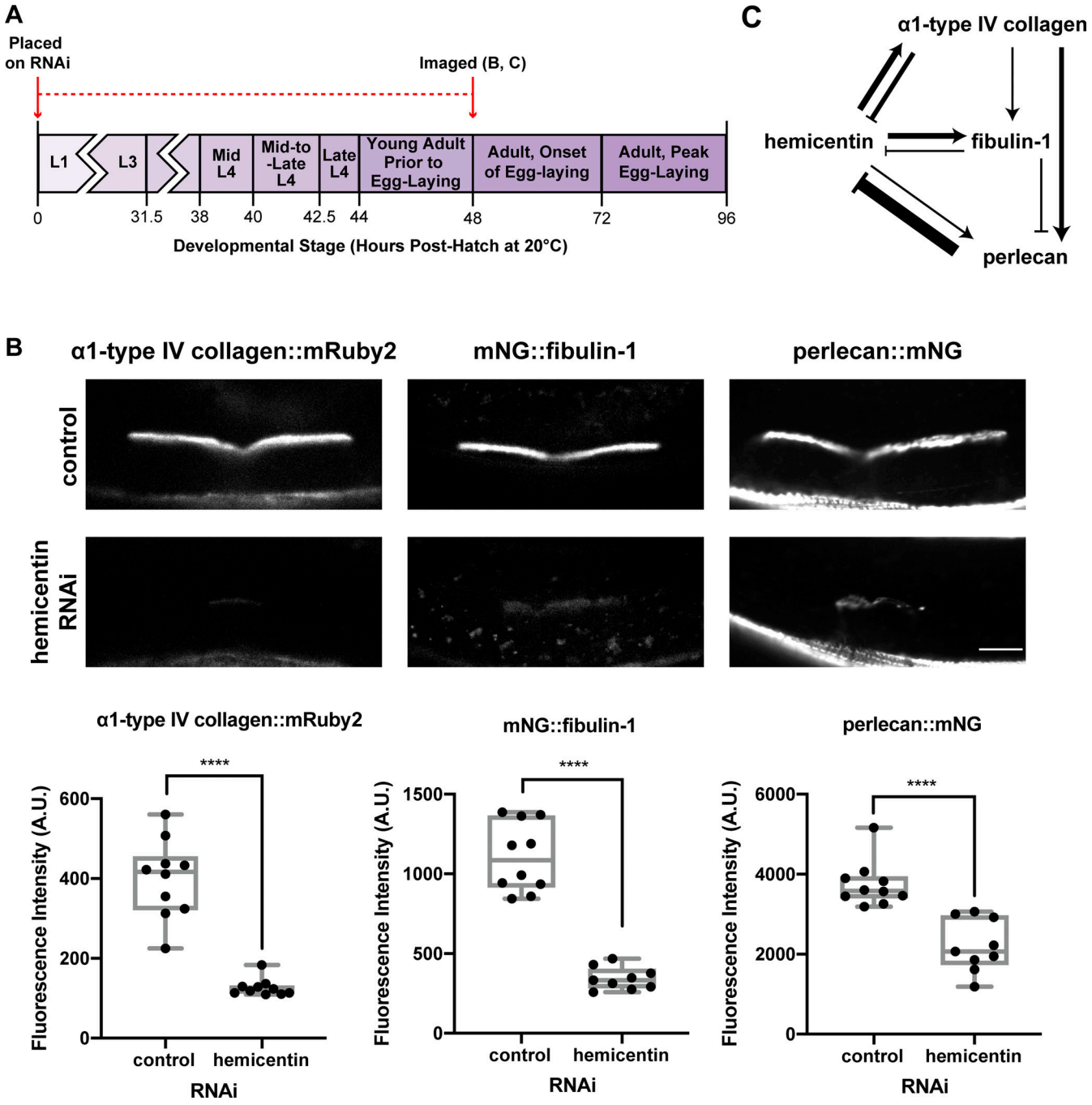

Figure 6. **Utse–seam B-LINK matrix component assembly is dependent on hemicentin. (A)** A diagram outlining timing of RNAi and imaging of utse–seam B-LINK matrix components. **(B)** Top: Fluorescence images of α1-type IV collagen::mRuby2, mNG::fibulin-1, and perlecan::mNG on control (T444T empty vector, *n* = 10 each) and hemicentin (*him-4*, *n* = 10 each) RNAi. Bottom: Mean fluorescence intensity of each component quantified. ****P < 0.0001, one-way ANOVA followed by post hoc Dunnet's test. Box edges in boxplots depict the 25th and 75th percentiles, the line in the box indicates the median value, and whiskers mark the minimum and maximum values. Scale bar, 10 µm. **(C)** A model of component recruitment to the utse–seam B-LINK. See Figs. S2 and S3 for further details.

the triple helix of collagen provides matrices with high tensile strength (Fidler et al., 2018). The role of collagen as a stabilizing component of BM–BM linkages may be conserved, as in mice and humans the collagen α3α4α5(IV) trimer localizes between the podocyte and glomerular BMs—fused BMs that resist strong hydrostatic pressure during blood filtration (Suleiman et al., 2013). Mutations in α3α4α5(IV) lead to Alport syndrome, a kidney disease that can result in kidney failure (Naylor et al., 2020). In Alport syndrome, the glomerular BM often splits into distinct podocyte and endothelial BMs, and it has been unclear why loss of α3α4α5(IV) collagen leads to BM separation (Naylor et al., 2020; Rumpelt, 1987). Our results suggest type IV collagen may help stably link the podocyte and endothelial BMs. Consistent with this idea, the α3α4α5(IV) trimer is thought to have

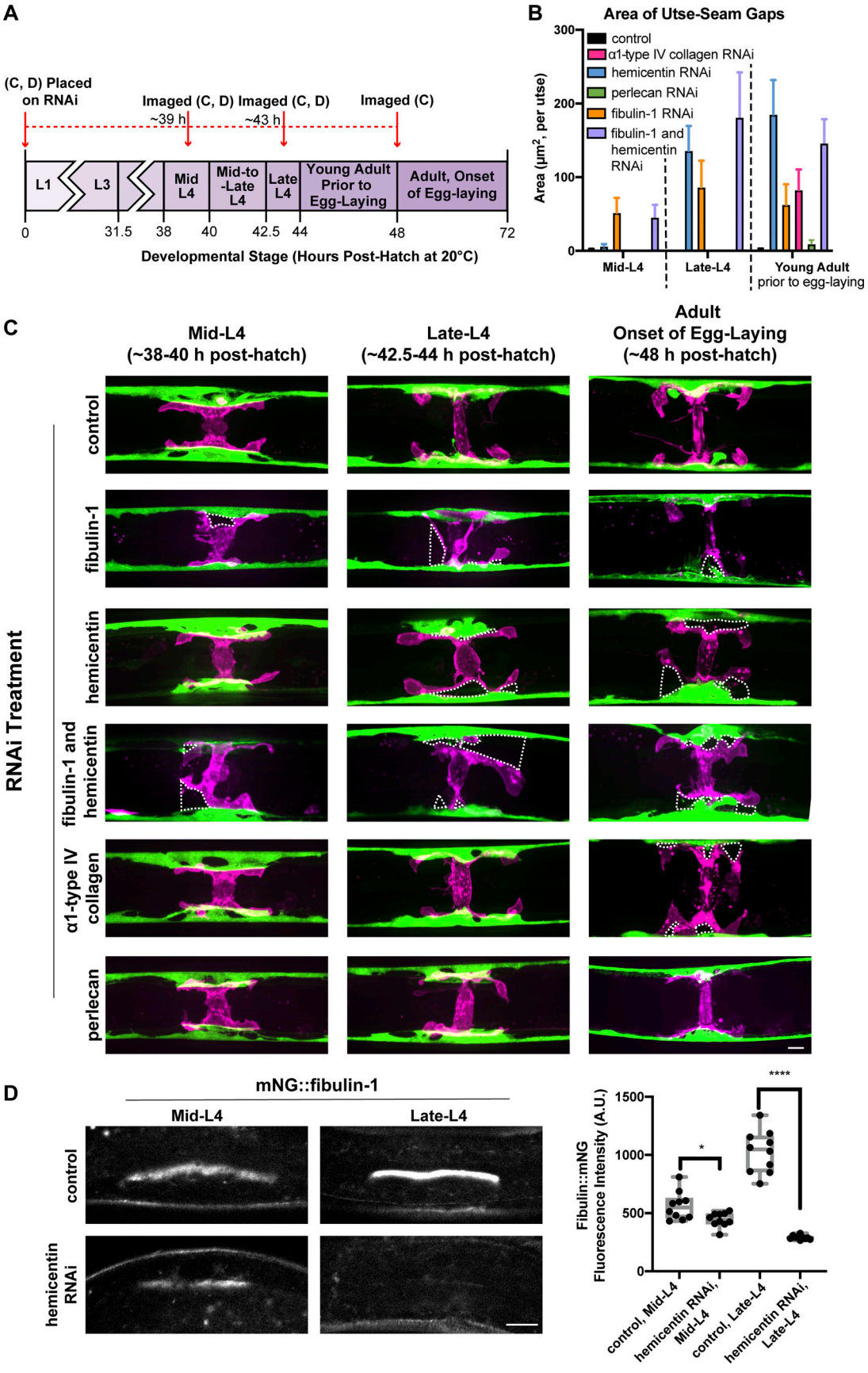

Figure 7. **Hemicentin and fibulin-1 initiate utse–seam BM–BM linkage, while type IV collagen maintains the B-LINK during egg-laying. (A)** A schematic outlining timing of RNAi and imaging of utse–seam cell association. **(B)** Quantification of the total utse–seam cell gap area per utse cell imaged in C. Error bars

represent SEM. **(C)** Ventral fluorescence images of the utse (magenta) and seam cells (green) at stages shown on control (L4440/T444T empty vectors, *n* = 10 each) and after RNAi-mediated reduction of B-LINK matrix components (*n* = 10 each). Regions where the utse has pulled away from the seam (utse–seam gaps) indicating defects in the B-LINK are highlighted with white dotted lines. **(D)** Left: Fluorescence images of mNG::fibulin-1 on control (T444T empty vector, *n* = 10 each) and hemicentin (*him-4*, *n* = 10 each) RNAi at the mid-L4 and late-L4 stages. Right: Quantification of mean fluorescence intensity at each stage on both control and hemicentin RNAi. Box edges in boxplots depict the 25th and 75th percentiles, the line in the box indicates the median value, and whiskers mark the minimum and maximum values. ****P < 0.0001, *P < 0.01 unpaired two-tailed Student's *t* test. Scale bars, 10 µm.

greater mechanical strength than that of the ubiquitously expressed α1α1α2(IV) trimer (Naylor et al., 2020). Notably, the collagen α3α4α5(IV) trimer is upregulated during glomerulogenesis and replaces the α1α1α2(IV) trimer at the time of BM–BM fusion (Abrahamson, 1985; Abrahamson et al., 2009). Whether this collagen also requires an earlier BM-bridging matrix is unknown. Loss of the two vertebrate hemicentins do not affect the glomerular BM in mice, however, fibulin-1 is present within the glomerular BM and might mediate the initial BM–BM connection (Lin et al., 2020; Naylor et al., 2020). The α3α4α5(IV) trimer is also present in the ear and eye, which are sites of BM–BM linkage that are also affected in Alport syndrome (Naylor et al., 2020; Keeley and Sherwood, 2019). Thus, type IV collagen may have a broad and important role in stably maintaining other BM–BM linkages.

Nearly 20 different BM–BM linkages have been observed that connect diverse tissues (Keeley and Sherwood, 2019; Gao et al., 2017; Welcker et al., 2021). Although the molecular nature of most of these connections remains elusive, the composition and structure of characterized BM–BM linkages are flexible. For example, the fibulin-1/hemicentin matrix that connects the pharyngeal and muscle BMs in *C. elegans* is 7–9 µm long, while the fibulin-1/hemicentin matrix at the utse–seam B-LINK is <0.1 µm (Vogel and Hedgecock, 2001). Matrix composition can also be distinct, as the anchor cell B-LINK harbors hemicentin, but lacks the fibulin-1, perlecan, and type IV collagen found at the utse–seam B-LINK. Yet, important commonalities in BM–BM linkages are also emerging, including the importance of hemicentins and fibulin-1 in *C. elegans* B-LINKs, zebrafish fin fold, and somite-epidermal BM–BM connections, and in stabilizing fine interdigitations of tendon at myotendinous junctions (Morrissey et al., 2014; Vogel and Hedgecock, 2001; Welcker et al., 2021; Muriel et al., 2005; Feitosa et al., 2012; Carney et al., 2010; Suleiman et al., 2013). Further commonalties include the role of type IV collagen in bridging the glomerular BM and utse–seam B-LINK BMs (Suleiman et al., 2013), where collagen may help resist high mechanical stress. Together, these studies suggest that BM–BM linkages can be tailored for the unique spatial, temporal, and mechanical needs of tissues. Understanding these linkages is important, as it will not only increase our knowledge of tissue structure and function, but also inform therapies to repair BM–BM connections in Alport syndrome and other pathologies affecting these ubiquitous, yet poorly studied tissue connections.

Materials and methods

Worm handling and strains

Worms were grown under standard conditions on nematode growth medium (NGM) agar plates seeded with OP50 *Escherichia coli* at 16, 18, or 20°C (Stiernagle, 2006). Strains used in this study are listed in Table S8.

Cloning of RNAi into T444T vector

For RNAi targeting *fbl-1* and *him-4*, new RNAi clones were generated using the T444T RNAi vector (Sturm et al., 2018). Briefly, PCR fragments corresponding to existing *fbl-1* and *him-4* RNAi clones in the Vidal (Rual et al., 2004) and Ahringer (Kamath et al., 2003) RNAi libraries, respectively, were amplified and inserted into SacII and HindIII-digested T444T vector by Gibson assembly. Forward and reverse primers used to amplify these fragments were: *fbl-1*, 5′-CGATGAATTCGAGCTCCA CCGCGGATGCATGTGACTCTGGTACAGA-3′ and 5′-GAGGTC GACGGTATCGATAAGCTTGTTCAACGAGTCGTGAATATAG-3′; *him-4*, 5′-CGATGAATTCGAGCTCCACCGCGGAACCAACAATTT CGTGGCTCAAAG-3′ and 5′-GAGGTCGACGGTATCGATAAGCTT TTCAGCCAATTTGATAGGGCAAGT-3′. Constructs were transformed into HT115 competent cells.

RNAi

All RNAi experiments were performed using the feeding method (Rual et al., 2004; Kamath et al., 2003; Timmons et al., 2001), and with the exception of *fbl-1* and *him-4*, all RNAi constructs were obtained from the Vidal and Ahringer libraries. RNAi bacterial cultures were grown in selective media (1:1,000 ampicillin) for 24 h at 30°C and then for an additional h after the addition of 1 mM IPTG to induce double-stranded RNA expression. RNAi plates were prepared by spreading a 1:1 mixture of 1M IPTG and 100 mg/ml ampicillin (18 µl each) on NGM agar plates. Plates were then seeded with RNAi bacterial cultures and left at room temperature overnight to allow for further induction and drying. For RNAi initiated at the L1 larval stage, synchronized L1 worms were placed on RNAi plates and allowed to feed between 24 and 120 h at 20°C depending on the experiment. The L4440 and T444T empty vectors were used as negative controls. For hemicentin and fibulin double knockdown, cultures of hemicentin and fibulin RNAi were grown normally and mixed in a 1:1 ratio prior to seeding.

For RNAi initiated at later developmental stages, worms were synchronized and plated on OP50, left to grow for ∼30, 35, 40, 45, or 48 h at 20°C, then transferred to RNAi plates. Briefly, worms were washed off of OP50 plates into 1 ml of M9 buffer and collected in 15-ml conical tubes, pelleted, and transferred into a non-stick polycarbonate 1.5-ml tube. Worms were washed 4× by centrifugation at 2,000 rpm for 60 s, aspirating supernatant, and resuspending in M9 buffer. After the second wash, tubes were placed on a rocking incubator for 10–15 min to allow worms to pass any bacteria remaining in the gut. Prior to the fourth and final wash, worms were transferred to a fresh 1.5-ml

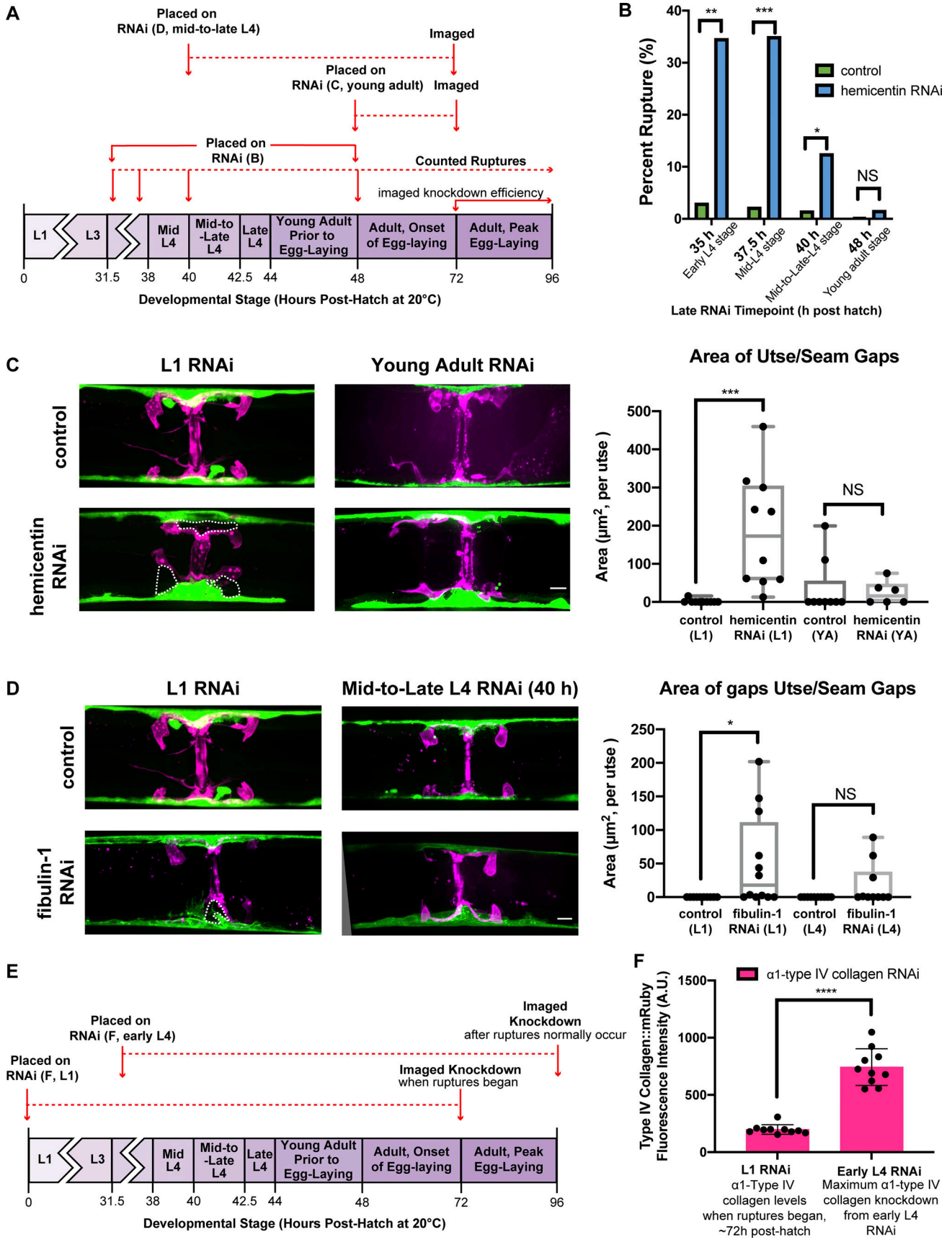

Figure 8. **Hemicentin is not required for later maintenance of the utse–seam B-LINK. (A)** A diagram detailing timing of RNAi and utse–seam connection analysis in B–D. **(B)** The percent of animals ruptured after 120 h on control (T444T empty vector) or hemicentin RNAi that was started at either the early-L4

(control n = 33, hemicentin n = 26), the mid-L4 (control n = 25, hemicentin n = 40), the late-L4 (control n = 26, hemicentin n = 48), or the young adult stage (control n = 243, hemicentin n = 127). ***P < 0.001, **P < 0.01, *P < 0.05, Fisher's Exact Tests. **(C)** Ventral fluorescence images of the utse (magenta) and seam (green) on hemicentin RNAi started at either the L1 stage or at the young adult (YA) stage (L1 data shown previously in Fig. 7, B and C). Regions where the utse has pulled away from the seam (utse–seam gaps) indicating defects in the B-LINK are highlighted with white dotted lines and quantified on the right (n = 10 each). ***P < 0.001, unpaired two-tailed Student's t tests. **(D)** Ventral fluorescence images of the utse and seam on fibulin-1 RNAi started at the L1 stage or at the mid-to-late-L4 stage (L1 data shown previously in Fig. 7, B and C). Utse–seam gaps (dotted lines) indicating defects in the B-LINK are quantified on the right (n = 10 each). *P < 0.05, unpaired two-tailed Student's t tests. **(E)** A schematic detailing timing of α1-type IV collagen RNAi in F. **(F)** Quantification of α1-type IV collagen::mRuby2 levels at the B-LINK when Rup phenotypes began after L1-initiated α1-type IV collagen RNAi compared to a1-type IV collagen::mRuby2 levels at the B-LINK after 120 h on α1-type IV collagen RNAi started at the early-L4 stage. Error bars represent SEM. ****P < 0.0001, unpaired two-tailed Student's t test. Box edges in boxplots depict the 25th and 75th percentiles, the line in the box indicates the median value, and whiskers mark the minimum and maximum values. Scale bars, 10 µm.

tube. After the final wash, worms were resuspended in M9 buffer and plated on RNAi-feeding plates.

Importantly, RNAi does not result in instantaneous protein loss, proteins can have different stabilities, and RNAi has different efficiencies in reducing mRNA. Thus, for RNAi experiments, reduction of levels of the targeted protein at the B-LINK was assessed to ensure sufficient knockdown was achieved. Knockdown levels were quantified and are shown in Tables S2, S3, S5, and S6. Box plots for all quantified knockdown experiments are in Fig. S5. To improve RNAi knockdown efficiency for the *fbl-1* RNAi, we used worms harboring a null mutation in *lin-35* (*lin-35n745*; Lehner et al., 2006).

Tissue-specific RNAi experiments were performed as previously described using *rrf-3*(*pk1426*) II; *qyIs102* [*fos-1ap::RDE-1, myo-2p::GFP*]; *qyIs10* [*lam-1p::lam-1::GFP*] IV; *rde-1*(*ne219*) V; *qyIs24* [*cdh-3p::mCherry::PLCdPH*] worms for uterine-specific RNAi and *rde-1*(*ne219*) V; *kzIs9*[*pKK1260*(*lin-26p::nls::gfp*), *pKK1253*(*lin-26p::rde-1*), *pRF4*(*rol-6*)] worms for hypodermal-specific RNAi (Qadota et al., 2007; Tabara et al., 1999; Hagedorn et al., 2009). Briefly, these worms harbor a null mutation in *rde-1* which is required for RNAi sensitivity (Qadota et al., 2007; Tabara et al., 1999). To restore RNAi sensitivity to the tissue of interest, a functional RDE-1 protein is specifically expressed in the tissue of interest allowing for tissue-specific RNAi knockdown.

Imaging

Confocal images were acquired at 20°C on a Zeiss AxioImager microscope equipped with a Yokogawa CSU-10 spinning-disc confocal controlled by Micromanager or Metamorph software using a Zeiss 40× Plan-APOCHROMAT 1.4NA oil immersion objective or 100× Plan-APOCHROMAT 1.4NA oil immersion objective and a Hamamatsu Orca-Fusion sCMOS camera or ImageEM EMCCD camera. Worms were mounted on 5% noble agar pads containing 0.01 M sodium azide for imaging all experiments except for Figs. 5 and 10. For Fig. 5, worms were mounted on 5% noble agar pads with no added anesthetic and added to agar pads in 3 µl undiluted 100-nm polystyrene bead solution (cat. #64010; Polysciences; Kim et al., 2013). For Fig. 10, worms were anesthetized by soaking in 5 mM Levamisole in M9 for 15 min (see FRAP details below).

Lateral images of B-LINK components were acquired using z-stacks at 0.37 µm intervals spanning the entirety of the B-LINK. For lateral and ventral images of the utse and seam, we acquired z-stacks spanning the top half of the utse (lateral) or the full depth of the utse (ventral).

For ventral images, slides were made by pouring agar onto a vinyl record to make agar pads with negative replicas of the record channels (Zhang et al., 2008). Worms were then added onto the record slides in M9, moved into the channels, and then a cover slip was placed over the worms (#M2000-10; Port City Diagnostics, Inc.). The cover slip was then gently pushed to rotate the animals in the channels to a ventral view for imaging.

Movies of animal rupture using the LITE-1 optogenetic strain to induce egg-laying were acquired at 20°C on a Zeiss Axio Zoom V16 stereo fluorescence microscope controlled by Zen 3.2 software using a 3× objective and an Axiocam digital camera. Movies were acquired using the Zen 3.2 movie recorder.

Images in Fig. 10 were acquired at 20°C on an inverted Zeiss 880 single-point scanning confocal attached to a Zeiss Axio Observer Z1 microscope, with Marzhauser linearly encoded stage and a 40× Plan-Neofluar 1.3NA oil immersion objective. Images were acquired sequentially by scanning bidirectionally at 0.34 micros using the galvanometer-based imaging mode, with a scan areal size of 106.3 × 106.3 µm in Zeiss Zen Black Acquisition software (version 3.3) and saved as CZI files. For all images the pinhole size was 39.2 µm, calculated at 1 arbitrary unit (A.U.) for 561 nm emission. mRuby2 fluorescent protein was excited with 561 nm laser, and emission was collected with GaAsP detector set to 565–650 nm range. To minimize general photobleaching due to image acquisition, 3 z-slices were acquired at 0.37-µm intervals, centered around the z-slice where the B-LINK was most in focus. A general photobleaching correction factor (detailed below) was applied to the pre-bleach and post-bleach images as shown in Fig. 10 to normalize to the respective 2-h post-bleach images.

FRAP

For FRAP experiments in Fig. 5, photobleaching was performed at 20°C using an iLas^2 FRAP system from BioVision equipped with an Omicron Lux 60 mW 405 nm continuous wave laser and controlled with MetaMorph software. Worms were immobilized using 100-nm polystyrene beads (cat. #64010; Polysciences) as described above. Regions of interest were selected with the freehand ROI tool. One half of the uterine–epidermal junction was photobleached at 10% laser power. The number of repetitions needed to achieve complete photobleaching varied by strain (number of repetitions varied between 20 and 50 reps, and total beach time ranged between 0.5 and 2.5 s) and was determined experimentally. After bleaching, images were acquired every 30 s for the first 5 min, every 2 min for the next

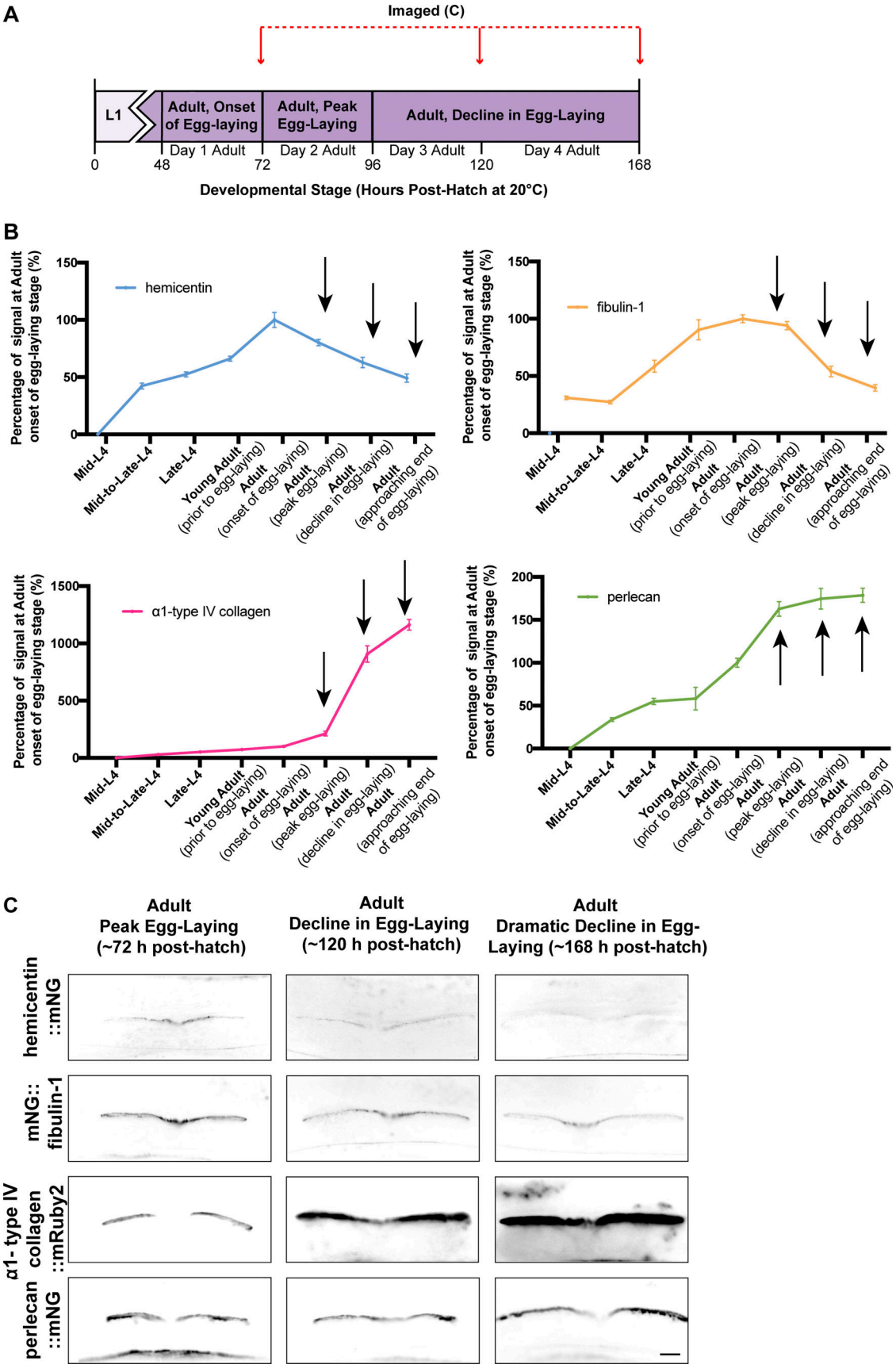

Figure 9. **Hemicentin and fibulin-1 decline at the utse–seam B-LINK during egg-laying. (A)** A schematic outlining when mNG::fibulin-1, hemicentin::mNG, α1-type IV collagen::mRuby2, and perlecan::mNG were imaged at the utse–seam B-LINK. **(B)** Quantification of mean florescence intensity of each B-LINK

matrix component from mid-L4 through adult decline in egg-laying stage as a percentage of the mean fluorescence intensity of that component in the onset of egg-laying adult (n = 10 all stages). Mid-L4 through onset of egg-laying data shown previously in Fig. 4 B. Black arrows indicate fluorescence time points shown in C. **(C)** Fluorescence images of hemicentin::mNG, mNG::fibulin-1, α1-type IV collagen::mRuby2, and perlecan::mNG at the B-LINK at the adult peak egg-laying, adult decline in egg-laying 120 h/~day 3 adult, and adult decline in egg-laying 168 h/~day 4 adult stages. Colors are inverted to improve visibility. Scale bars, 10 µm.

10 min, and then once more after the next 15 min. Animals were rescued after photobleaching to confirm they were able to recover and continue developing.

FRAP experiments in Fig. 10 were completed at 20°C on an inverted Zeiss 880 single-point scanning confocal attached to a Zeiss Axio Observer Z1 microscope, with Marzhauser linearly encoded stage and a 40× Plan-Neofluar 1.3NA oil immersion objective. Worms were anesthetized by soaking in 5 mM Levamisole in M9 for 15 min, and then transferred to a small (1 × 1 cm) 4% noble agar pad. A glass cover slip (thickness 0.15–0.19 mm) was then placed on top, sealed with valap (equal weight vaseline, lanolin, and paraffin), and flooded with 5 mM Levamisole. The sealed coverslip prevented the slide from drying out to allow for longer time lapsing without rescue (see Kelley et al., 2017 for details). For all images, the pinhole size was 39.2 µm, calculated at 1 A.U. for 561 nm emission. mRuby2 fluorescent protein was excited with 561 nm laser and emission was collected with GaAsP detector set to 565–650 nm range. A rectangle region in one arm of the BLINK was photobleached using 30 iterations of simultaneous 405 nm (100% laser power) and 561 (100% laser power) for a total bleaching time of 1.5 s. Worms were imaged prior and immediately following bleaching, then again 2 h later. ADAMTS9/20 (GON-1) knockdown was calculated at the time of imaging and found to be 99.8% (Control L4440 RNAi n = 11, GON-1 RNAi n = 8).

Image analysis, processing, and quantification

Raw images were quantified in Fiji 2.0 (Schindelin et al., 2012). B-LINK fluorescence intensity measurements were acquired by taking the mean fluorescence intensity of a 3-pixel-wide line drawn through the left side of the B-LINK in a single confocal z-slice. Background intensity values were obtained by taking a line measurement in a region with no visible fluorescence signal. Images of the utse and seam markers were acquired as z-stacks and are displayed in figures as max projections. Images of collagen::mRuby2 fluorescence recovery in control and ADAMTS9/20 RNAi treated animals were acquired as z-stacks and displayed in Fig. 10 C as sum projections. All other images are single slices. All images of each strain within each experiment were acquired using identical settings. Fluorescence intensity values for the adult timepoints in Fig. 9 B were normalized to data in Fig. 4 B based on the overlapping adult peak egg-laying timepoint. For the data in Fig. 10 B, a bleach correction factor was calculated to account for general photobleaching during image acquisition across the duration of the experiment. Briefly, the background-corrected fluorescence intensity measurement on the side of the B-LINK where FRAP was not performed at the 2-h post-bleach timepoint was divided by the respective value at the pre-bleach timepoint to obtain the bleach correction factor. Fluorescence intensity measurements at the pre-bleach and post-bleach timepoints on the side of the B-LINK where FRAP was performed were then multiplied by the respective bleach correction factor to normalize these values to the 2-h post-bleach fluorescence intensity measurement in the same region.

3D isosurfaces of the utse and B-LINK hemicentin were created from confocal z-stacks and exported using Imaris 7.4. Figures were constructed using Adobe Illustrator (CC 2021), and graphs were exported from GraphPad Prism 8.

Scoring of Rup phenotype

To score for the Rup phenotype, ~30–80 worms were plated on RNAi at the L1, L3, L4, or young adult stages as described above. After 24 h on RNAi, the number of worms on the plate was recorded. At least once every 24 h for the next 120 h, plates were visually screened for ruptured worms. Ruptured animals were subtracted from the total number of starting animals and picked off the plate so as not to double count them. After 120 h, the percentage of ruptured animals was calculated and compared to controls using Fisher's exact test.

For the long-term collagen RNAi rupture experiment, worms were synchronized and plated on RNAi at the young adult stage as previously described. Plates were then scored for ruptures as above for 7 d (168 h). Each day, non-ruptured worms were picked onto fresh RNAi plates to avoid starvation and remove progeny. After 7 d, the percentage of ruptured animals was calculated and compared to controls using Fisher's exact test.

For experiments using the optogenetically induced muscle contraction strain KG1271, worms were synchronized and plated on RNAi at the L1 stage as described above and fed for 72 h. Plates of animals were placed on the Axio Zoom V.16 where they were exposed to 488 nm light for ~7 s. After light-induced muscle contraction, the number of eggs expelled by the animal was recorded and the animal was scored as positive or negative for the Rup phenotype.

Rup phenotype screen

A list of genes documented to cause the Rup phenotype was compiled using WormBase (http://wormbase.org; Table S7). The list was generated using the WormMine feature, which returns all genes annotated to a particular phenotype (RNAi/allele). These 403 genes were then filtered by whether they encoded proteins with a signal sequence (secreted or transmembrane proteins), which resulted in a list of 52 genes. To further filter this list, genes that are unlikely to be directly involved in collagen recruitment were removed. This included genes encoding proteins with roles in metabolism, the cuticle, or gap junctions. We also removed matrix proteins previously tested for roles in the B-LINK. Furthermore, we focused on genes that met one or more of the following criteria: (1) genes that on their own caused

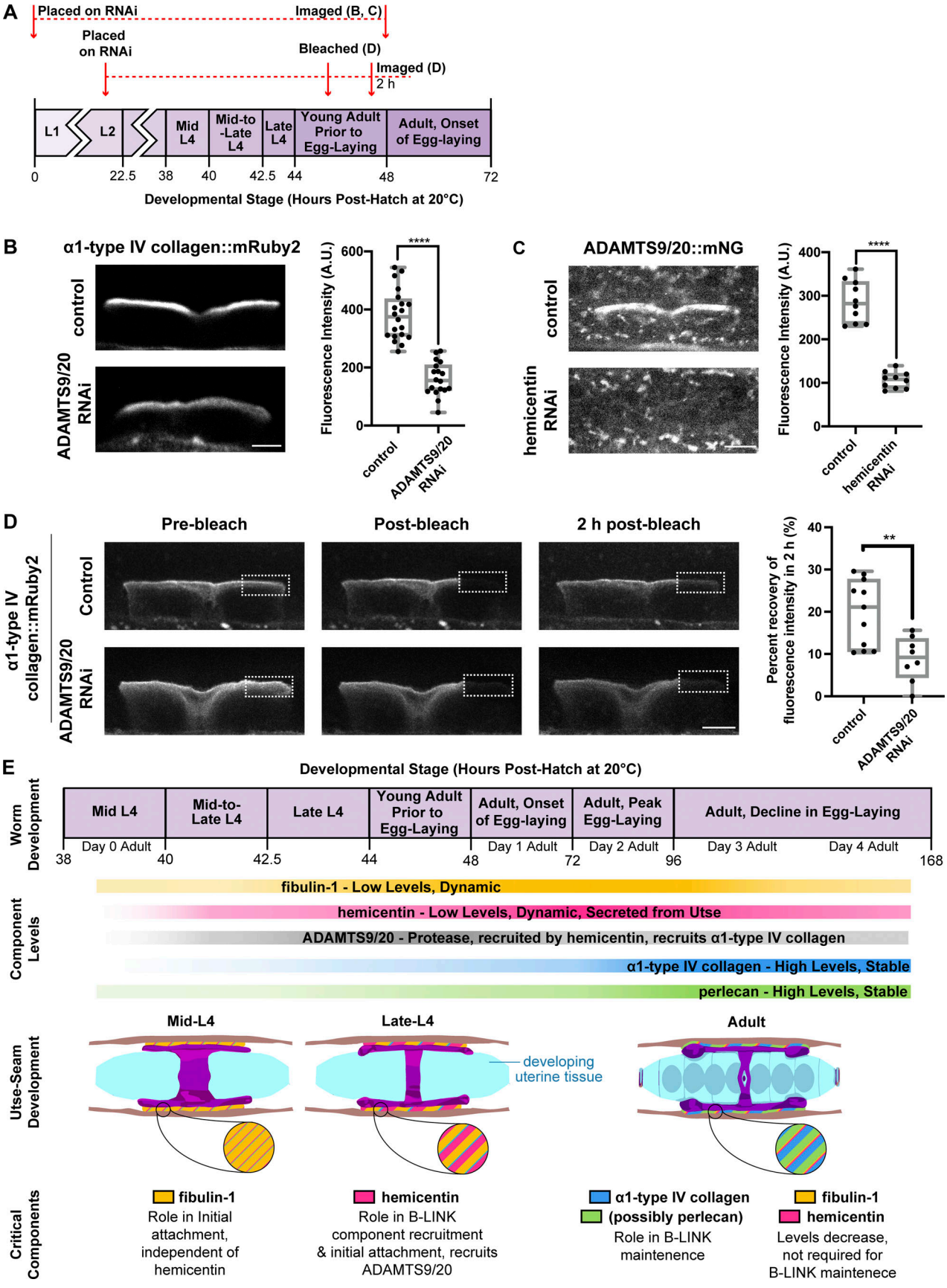

Figure 10. **ADAMTS9/20 promotes type IV collagen assembly at the B-LINK. (A)** A diagram showing when animals were photobleached and imaged. **(B)** Left: Fluorescence images of a1-type IV collagen::mRuby2 on control (L4440 empty vector, *n* = 10 each) and ADAMTS9/20 (*gon-1*, *n* = 10 each) RNAi. Right:

Mean fluorescence intensity of each component quantified. ****P < 0.0001, unpaired two-tailed Student's *t* test. **(C)** Left: Fluorescence images of ADAMTS9/20::mNG on control (T444T empty vector, *n* = 10 each) and hemicentin (*him-4*, *n* = 10 each) RNAi. Right: Mean fluorescence intensity of each component quantified. ****P < 0.0001, unpaired two-tailed Student's *t* test. **(D)** Left: Fluorescence images of α1-type IV collagen::mRuby2 before photobleaching, immediately after photobleaching, and 2 h post-photobleaching in young adult animals. Images were corrected to account for general bleaching over the course of the experiment (Materials and methods). Dotted white box indicates bleached region. Right: A boxplot showing the mean percent recovery of α1-type IV collagen::mRuby2 in the young adult B-LINK after 2 h (*n* = 11 control, *n* = 8 ADAMTS9/20 RNAi). Values were normalized to an unbleached region of the B-LINK to account for general photobleaching. **P < 0.01, unpaired two-tailed Student's *t* test. **(E)** A model for assembly and role of different matrix components at the utse–seam B-LINK. Box edges in boxplots depict the 25th and 75th percentiles, the line in the box indicates the median value, and whiskers mark the minimum and maximum values. Scale bars, 10 µm.

a Rup phenotype (not a synthetic interaction), (2) genes documented to be expressed in the utse or hypodermis, (3) genes whose loss is also documented to cause sterility or reduced brood size similar to known B-LINK components, and (4) genes whose RNAi loss was not pleotropic and primarily led to a Rup phenotype. This filtering process left us with a list of 11 genes that were then screened using RNAi clones from either the Ahringer or Vidal libraries.

Statistical analysis

Statistical analysis was performed in GraphPad Prism 8. Distribution of data was assessed for normality using the Shapiro–Wilk test. For comparisons of mean fluorescence intensities between two populations, we used an unpaired two-tailed Student's *t* test. To compare mean fluorescence intensities between three or more populations, we performed a one-way ANOVA followed by either a post hoc Dunnett's or Tukey's multiple comparison test. To compare percentage rupture between two populations, we performed a Fisher's Exact Test. All graphs were prepared in GraphPad Prism. Figure legends indicate sample sizes, statistical tests used, and P values.

Online supplemental material

Fig. S1, related to Fig. 4, shows the identified B-LINK matrix components that are enriched at the utse–seam B-LINK at the B-LINK underneath the anchor cell. Fig. S2, related to Fig. 6, shows fluorescence intensity of hemicentin (HIM-4::mNG) on control (L4440/T444T empty vectors) and corresponding B-LINK component RNAi (α1-type IV collagen, perlecan, and fibulin-1). Fig. S3, also related to Fig. 6, shows fluorescence intensity of other B-LINK components (α1-type IV collagen::mRuby2, mNG::fibulin-1, and perlecan::mNG) on control (L4440/T444T empty vectors) and corresponding B-LINK component RNAi (hemicentin, α1-typeIV collagen, perlecan, and fibulin-1). Fig. S4, related to Fig. 10, shows further characterization of GON-1 (referred to as ADAMTS9/20, the vertebrate ortholog pair) including a developmental time course, fluorescence intensity of ADAMTS9/20 on B-LINK component RNAi, and fluorescence intensity of other B-LINK components on ADAMTS9/20 RNAi. Fig. S5, related to Figs. 3, 6, 7, and 8, shows box plots of all RNAi knockdown experiments completed with B-LINK component RNAi at various timepoints. Table S1, related to Fig. 3, shows percentage rupture of all screened matrix components. Table S2, related to Figs. 3, 6, 7, and 8, shows percentage knockdown for L1 RNAi experiments. Table S3, related to Table S1, shows percentage knockdown for L3 RNAi experiments. Table S4, related to Table S1, shows rupture screening with the uterine-specific and hypodermal-specific RNAi. Table S5, related to Fig. 8, shows percentage knockdown for L4 RNAi experiments where ruptures were scored. Table S6, related to Fig. 8, shows percentage knockdown for L4 RNAi experiments where the utse and seam were imaged. Table S7, related to Fig. 10, shows the full list of genes identified to cause the Rup phenotype. Table S8 lists all strains used in this study. Video 1 shows hemicentin located at the utse–seam B-LINK. Video 2 shows optogenetically induced muscle contraction causes egg-laying. Video 3 shows optogenetically induced muscle contraction causes uterine rupture after loss of hemicentin.

Acknowledgments

We thank S.G. Payne and A. Garde for comments on the manuscript and members of the Sherwood laboratory for helpful discussions. We thank A. Kawska (info@illuscientia.com) for work on schematics. We thank L. Cameron and the Duke Light Microscopy Core Facility for microscopy support.

C.A. Gianakas was supported by National Institutes of Health grant F31HL156438, and D.R. Sherwood, C.A. Gianakas, D.P. Keeley, W. Ramos-Lewis, K. Park, R. Jayadev, and Q. Chi were supported by R35GM118049, R21OD032430, and R21OD028766.

The authors declare no competing financial interests.

Author contributions: D.P. Keeley, C.A. Gianakas, and D.R. Sherwood conceived the project. C.A. Gianakas designed, completed, and analyzed all experiments with the following additional contributions: Q. Chi built RNAi constructs used in Figs. 3, 6, 7, and 8, Figs. S2, S3, and S5, Tables S1, S2, S3, S4, S5, and S6; K. Park acquired and analyzed the utse/seam time-course data used in Fig. 1 C and Fig. 2 A and collected the anchor cell data shown in Fig. S1; W. Ramos-Lewis acquired and analyzed the B-LINK component time course shown in Fig. 9, B and C; D.P. Keeley acquired a portion of the rupture data shown in Table S1 and compiled the Rup list shown in Table S7; R. Jayadev built the RNAi-sensitized strains used in Figs. 7 and 8, Figs. S2, S3, S4, and S5, and Tables S1, S2, S3, and S6. R. Jayadev also completed the uterine and hypodermal specific RNAi experiments in Table S4. I.W. Kenny and R. Jayadev collected the FRAP data shown in Fig. 10 C. C.A. Gianakas prepared the figures. C.A. Gianakas and D.R. Sherwood wrote the initial manuscript. C.A. Gianakas, D.R. Sherwood, D.P. Keeley, K. Park, W. Ramos-Lewis, and R. Jayadev reviewed and edited the manuscript.

Submitted: 17 December 2021
Revised: 16 August 2022
Accepted: 26 September 2022

References

Abrahamson, D.R. 1985. Origin of the glomerular basement membrane visualized after in vivo labeling of laminin in newborn rat kidneys. *J. Cell Biol.* 100:1988–2000. https://doi.org/10.1083/jcb.100.6.1988

Abrahamson, D.R., B.G. Hudson, L. Stroganova, D.-B. Borza, and P.L. St John. 2009. Cellular origins of type IV collagen networks in developing glomeruli. *J. Am. Soc. Nephrol.* 20:1471–1479. https://doi.org/10.1681/ASN.2008101086

Brown, N.H. 2011. Extracellular matrix in development: Insights from mechanisms conserved between invertebrates and vertebrates. *Cold Spring Harb. Perspect. Biol.* 3. https://doi.org/10.1101/cshperspect.a005082

Carney, T.J., N.M. Feitosa, C. Sonntag, K. Slanchev, J. Kluger, D. Kiyozumi, J.M. Gebauer, J. Coffin Talbot, C.B. Kimmel, K. Sekiguchi, et al. 2010. Genetic analysis of fin development in zebrafish identifies furin and hemicentin1 as potential novel fraser syndrome disease genes. *PLoS Genet.* 6:e1000907. https://doi.org/10.1371/journal.pgen.1000907

Clay, M.R., and D.R. Sherwood. 2015. Basement membranes in the worm: A dynamic scaffolding that instructs cellular behaviors and shapes tissues. *Curr. Top. Membr.* 76:337–371. https://doi.org/10.1016/bs.ctm.2015.08.001

Edwards, S.L., N.K. Charlie, M.C. Milfort, B.S. Brown, C.N. Gravlin, J.E. Knecht, and K.G. Miller. 2008. A novel molecular solution for ultraviolet light detection in *Caenorhabditis elegans*. *PLoS Biol.* 6:e198. https://doi.org/10.1371/journal.pbio.0060198

Feitosa, N.M., J. Zhang, T.J. Carney, M. Metzger, V. Korzh, W. Bloch, and M. Hammerschmidt. 2012. Hemicentin 2 and Fibulin 1 are required for epidermal-dermal junction formation and fin mesenchymal cell migration during zebrafish development. *Dev. Biol.* 369:235–248. https://doi.org/10.1016/j.ydbio.2012.06.023

Fidler, A.L., S.P. Boudko, A. Rokas, and B.G. Hudson. 2018. The triple helix of collagens: An ancient protein structure that enabled animal multicellularity and tissue evolution. *J. Cell Sci.* 131:jcs203950. https://doi.org/10.1242/jcs.203950

Gally, C., H. Zhang, and M. Labouesse. 2016. Functional and genetic analysis of VAB-10 spectraplakin in *Caenorhabditis elegans*. *Methods Enzymol.* 569: 407–430. https://doi.org/10.1016/bs.mie.2015.05.005

Gao, Y., D. Mruk, H. Chen, W.-Y. Lui, W.M. Lee, and C.Y. Cheng. 2017. Regulation of the blood-testis barrier by a local axis in the testis: Role of laminin α2 in the basement membrane. *FASEB J.* 31:584–597. https://doi.org/10.1096/fj.201600870R

Ghosh, S., and P.W. Sternberg. 2014. Spatial and molecular cues for cell outgrowth during *C. elegans* uterine development. *Dev. Biol.* 396:121–135. https://doi.org/10.1016/j.ydbio.2014.09.028

Gordon, K.L., S.G. Payne, L.M. Linden-High, A.M. Pani, B. Goldstein, E.J.A. Hubbard, and D.R. Sherwood. 2019. Ectopic germ cells can induce niche-like enwrapment by neighboring body wall muscle. *Curr. Biol.* 29: 823–833.e5. https://doi.org/10.1016/j.cub.2019.01.056

Hagedorn, E.J., H. Yashiro, J.W. Ziel, S. Ihara, Z. Wang, and D.R. Sherwood. 2009. Integrin acts upstream of netrin signaling to regulate formation of the anchor cell's invasive membrane in *C. elegans*. *Dev. Cell.* 17: 187–198. https://doi.org/10.1016/j.devcel.2009.06.006

Hagedorn, E.J., J.W. Ziel, M.A. Morrissey, L.M. Linden, Z. Wang, Q. Chi, S.A. Johnson, and D.R. Sherwood. 2013. The netrin receptor DCC focuses invadopodia-driven basement membrane transmigration in vivo. *J. Cell Biol.* 201:903–913. https://doi.org/10.1083/jcb.201301091

Hesselson, D., C. Newman, K.W. Kim, and J. Kimble. 2004. GON-1 and fibulin have antagonistic roles in control of organ shape. *Curr. Biol.* 14: 2005–2010. https://doi.org/10.1016/j.cub.2004.11.006

Hohenester, E., and P.D. Yurchenco. 2013. Laminins in basement membrane assembly. *Cell Adhes. Migrat.* 7:56–63. https://doi.org/10.4161/cam.21831

Jayadev, R., Q. Chi, D.P. Keeley, E.L. Hastie, L.C. Kelley, and D.R. Sherwood. 2019. α-Integrins dictate distinct modes of type IV collagen recruitment to basement membranes. *J. Cell Biol.* 218:3098–3116. https://doi.org/10.1083/jcb.201903124

Jayadev, R., M.R.P.T. Morais, J.M. Ellingford, S. Srinivasan, R.W. Naylor, C. Lawless, A.S. Li, J.F. Ingham, E. Hastie, Q. Chi, et al. 2022. A basement membrane discovery pipeline uncovers network complexity, regulators, and human disease associations. *Sci. Adv.* 8:eabn2265. https://doi.org/10.1126/sciadv.abn2265

Jayadev, R., and D.R. Sherwood. 2017. Basement membranes. *Curr. Biol.* 27: R207–R211. https://doi.org/10.1016/j.cub.2017.02.006

Kamath, R.S., A.G. Fraser, Y. Dong, G. Poulin, R. Durbin, M. Gotta, A. Kanapin, N. Le Bot, S. Moreno, M. Sohrmann, et al. 2003. Systematic functional analysis of the *Caenorhabditis elegans* genome using RNAi. *Nature.* 421: 231–237. https://doi.org/10.1038/nature01278

Kawano, T., H. Zheng, D.C. Merz, Y. Kohara, K.K. Tamai, K. Nishiwaki, and J.G. Culotti. 2009. *C. elegans* mig-6 encodes papilin isoforms that affect distinct aspects of DTC migration, and interacts genetically with mig-17 and collagen IV. *Development.* 136:1433–1442. https://doi.org/10.1242/dev.028472

Keeley, D.P., E. Hastie, R. Jayadev, L.C. Kelley, Q. Chi, S.G. Payne, J.L. Jeger, B.D. Hoffman, and D.R. Sherwood. 2020. Comprehensive endogenous tagging of basement membrane components reveals dynamic movement within the matrix scaffolding. *Dev. Cell.* 54:60–74.e7. https://doi.org/10.1016/j.devcel.2020.05.022

Keeley, D.P., and D.R. Sherwood. 2019. Tissue linkage through adjoining basement membranes: The long and the short term of it. *Matrix Biol.* 75–76:58–71. https://doi.org/10.1016/j.matbio.2018.05.009

Kelley, L.C., Z. Wang, E.J. Hagedorn, L. Wang, W. Shen, S. Lei, S.A. Johnson, and D.R. Sherwood. 2017. Live-cell confocal microscopy and quantitative 4D image analysis of anchor-cell invasion through the basement membrane in *Caenorhabditis elegans*. *Nat. Protoc.* 12:2081–2096. https://doi.org/10.1038/nprot.2017.093

Kelwick, R., I. Desanlis, G.N. Wheeler, and D.R. Edwards. 2015. The ADAMTS (A disintegrin and metalloproteinase with thrombospondin motifs) family. *Genome Biol.* 16:113. https://doi.org/10.1186/s13059-015-0676-3

Kim, E., L. Sun, C.V. Gabel, and C. Fang-Yen. 2013. Long-term imaging of *Caenorhabditis elegans* using nanoparticle-mediated immobilization. *PLoS One.* 8:e53419. https://doi.org/10.1371/journal.pone.0053419

Kocsisova, Z., K. Kornfeld, and T. Schedl. 2019. Rapid population-wide declines in stem cell number and activity during reproductive aging in *C. elegans*. *Development.* 146:dev173195. https://doi.org/10.1242/dev.173195

Kramer, J.M. 2005. Basement membranes. *WormBook*:1–15. https://doi.org/10.1895/wormbook.1.16.1

Lehner, B., A. Calixto, C. Crombie, J. Tischler, A. Fortunato, M. Chalfie, and A.G. Fraser. 2006. Loss of LIN-35, the *Caenorhabditis elegans* ortholog of the tumor suppressor p105Rb, results in enhanced RNA interference. *Genome Biol.* 7:R4. https://doi.org/10.1186/gb-2006-7-1-r4

Li, S., Y. Qi, K. McKee, J. Liu, J. Hsu, and P.D. Yurchenco. 2017. Integrin and dystroglycan compensate each other to mediate laminin-dependent basement membrane assembly and epiblast polarization. *Matrix Biol.* 57–58:272–284. https://doi.org/10.1016/j.matbio.2016.07.005

Lin, M.-H., B.D. Pope, T. Sasaki, D.P. Keeley, D.R. Sherwood, and J.H. Miner. 2020. Mammalian hemicentin 1 is assembled into tracks in the extracellular matrix of multiple tissues. *Dev. Dynam.* 249:775–788. https://doi.org/10.1002/dvdy.159

Makanya, A., A. Anagnostopoulou, and V. Djonov. 2013. Development and remodeling of the vertebrate blood-gas barrier. *Biomed Res. Int.* 2013: 101597. https://doi.org/10.1155/2013/101597

Matsubayashi, Y., B.J. Sánchez-Sánchez, S. Marcotti, E. Serna-Morales, A. Dragu, M.-D.-C. Díaz-de-la-Loza, G. Vizcay-Barrena, R.A. Fleck, and B.M. Stramer. 2020. Rapid homeostatic turnover of embryonic ECM during tissue morphogenesis. *Dev. Cell.* 54:33–42.e9. https://doi.org/10.1016/j.devcel.2020.06.005

Morrissey, M.A., D.P. Keeley, E.J. Hagedorn, S.T.H. McClatchey, Q. Chi, D.H. Hall, and D.R. Sherwood. 2014. B-LINK: A hemicentin, plakin, and integrin-dependent adhesion system that links tissues by connecting adjacent basement membranes. *Dev. Cell.* 31:319–331. https://doi.org/10.1016/j.devcel.2014.08.024

Muriel, J.M., C. Dong, H. Hutter, and B.E. Vogel. 2005. Fibulin-1C and Fibulin-1D splice variants have distinct functions and assemble in a hemicentin-dependent manner. *Development.* 132:4223–4234. https://doi.org/10.1242/dev.02007

Muriel, J.M., C. Dong, and B.E. Vogel. 2012. Distinct regions within fibulin-1D modulate interactions with hemicentin. *Exp. Cell Res.* 318:2543–2547. https://doi.org/10.1016/j.yexcr.2012.08.007

Naylor, R.W., M.R.P.T. Morais, and R. Lennon. 2021. Complexities of the glomerular basement membrane. *Nat. Rev. Nephrol.*. 17:112–127. https://doi.org/10.1038/s41581-020-0329-y

Newman, A.P., J.G. White, and P.W. Sternberg. 1996. Morphogenesis of the *C. elegans* hermaphrodite uterus. *Development.* 122:3617–3626. https://doi.org/10.1242/dev.122.11.3617

Obermeier, B., R. Daneman, and R.M. Ransohoff. 2013. Development, maintenance and disruption of the blood-brain barrier. *Nat. Med.* 19: 1584–1596. https://doi.org/10.1038/nm.3407

Qadota, H., M. Inoue, T. Hikita, M. Köppen, J.D. Hardin, M. Amano, D.G. Moerman, and K. Kaibuchi. 2007. Establishment of a tissue-specific RNAi system in *C. elegans*. *Gene.* 400:166–173. https://doi.org/10.1016/j.gene.2007.06.020

Ravi, B., J. Garcia, and K.M. Collins. 2018. Homeostatic feedback modulates the development of two-state patterned activity in a model serotonin motor circuit in *Caenorhabditis elegans*. *J. Neurosci.* 38:6283–6298. https://doi.org/10.1523/JNEUROSCI.3658-17.2018

Rogalski, T.M., E.J. Gilchrist, G.P. Mullen, and D.G. Moerman. 1995. Mutations in the unc-52 gene responsible for body wall muscle defects in adult *Caenorhabditis elegans* are located in alternatively spliced exons. *Genetics*. 139:159–169. https://doi.org/10.1093/genetics/139.1.159

Rual, J.-F., J. Ceron, J. Koreth, T. Hao, A.-S. Nicot, T. Hirozane-Kishikawa, J. Vandenhaute, S.H. Orkin, D.E. Hill, S. van den Heuvel, and M. Vidal. 2004. Toward improving *Caenorhabditis elegans* phenome mapping with an ORFeome-based RNAi library. *Genome Res.* 14:2162–2168. https://doi.org/10.1101/gr.2505604

Rumpelt, H.J. 1987. Alport's syndrome: Specificity and pathogenesis of glomerular basement membrane alterations. *Pediatr. Nephrol.* 1:422–427. https://doi.org/10.1007/BF00849248

Schafer, W.F. 2006. Genetics of egg-laying in worms. *Annu. Rev. Genet.* 40: 487–509. https://doi.org/10.1146/annurev.genet.40.110405.090527

Schindelin, J., I. Arganda-Carreras, E. Frise, V. Kaynig, M. Longair, T. Pietzsch, S. Preibisch, C. Rueden, S. Saalfeld, B. Schmid, et al. 2012. Fiji: An open-source platform for biological-image analysis. *Nat. Methods*. 9: 676–682. https://doi.org/10.1038/nmeth.2019

Schindler, A.J., and D.R. Sherwood. 2013. Morphogenesis of the caenorhabditis elegans vulva. *Wiley Interdiscip. Rev. Dev. Biol.* 2:75–95. https://doi.org/10.1002/wdev.87

Sherwood, D.R., and P.W. Sternberg. 2003. Anchor cell invasion into the vulval epithelium in *C. elegans*. *Dev. Cell.* 5:21–31. https://doi.org/10.1016/s1534-5807(03)00168-0

Sixt, M., B. Engelhardt, F. Pausch, R. Hallmann, O. Wendler, and L.M. Sorokin. 2001. Endothelial cell laminin isoforms, laminins 8 and 10, play decisive roles in T cell recruitment across the blood-brain barrier in experimental autoimmune encephalomyelitis. *J. Cell Biol.* 153:933–946. https://doi.org/10.1083/jcb.153.5.933

Stevens, L.J., and A. Page-McCaw. 2012. A secreted MMP is required for re-epithelialization during wound healing. *Mol. Biol. Cell*. 23:1068–1079. https://doi.org/10.1091/mbc.E11-09-0745

Stiernagle, T. 2006. Maintenance of *C. elegans*. *WormBook*. 1–11. https://doi.org/10.1895/wormbook.1.101.1

Sturm, Á., É.K. SaskoiTibor, N. Weinhardt, and T. Vellai. 2018. Highly efficient RNAi and Cas9-based auto-cloning systems for *C. elegans* research. *Nucleic Acids Res.* 46:e105. https://doi.org/10.1093/nar/gky516

Suleiman, H., L. Zhang, R. Roth, J.E. Heuser, J.H. Miner, A.S. Shaw, and A. Dani. 2013. Nanoscale protein architecture of the kidney glomerular basement membrane. *Elife*. 2:e01149. https://doi.org/10.7554/eLife.01149

Tabara, H., M. Sarkissian, W.G. Kelly, J. Fleenor, A. Grishok, L. Timmons, A. Fire, and C.C. Mello. 1999. The rde-1 gene, RNA interference, and transposon silencing in *C. elegans*. *Cell*. 99:123–132. https://doi.org/10.1016/s0092-8674(00)81644-x

Timmons, L., D.L. Court, and A. Fire. 2001. Ingestion of bacterially expressed dsRNAs can produce specific and potent genetic interference in *Caenorhabditis elegans*. *Gene*. 263:103–112. https://doi.org/10.1016/s0378-1119(00)00579-5

Vaccaro, C.A., and J.S. Brody. 1981. Structural features of alveolar wall basement membrane in the adult rat lung. *J. Cell Biol.* 91:427–437. https://doi.org/10.1083/jcb.91.2.427

Vogel, B.E., and E.M. Hedgecock. 2001. Hemicentin, a conserved extracellular member of the immunoglobulin superfamily, organizes epithelial and other cell attachments into oriented line-shaped junctions. *Development*. 128:883–894. https://doi.org/10.1242/dev.128.6.883

Welcker, D., C. Stein, N.M. Feitosa, J. Armistead, J.-L. Zhang, S. Lütke, A. Kleinridders, J.C. Brüning, S.A. Eming, G. Sengle, et al. 2021. Hemicentin-1 is an essential extracellular matrix component of the dermal-epidermal and myotendinous junctions. *Sci. Rep.* 11:17926. https://doi.org/10.1038/s41598-021-96824-4

Zhang, J.-L., S. Richetti, T. Ramezani, D. Welcker, S. Lütke, H.-M. Pogoda, J. Hatzold, F. Zaucke, D.R. Keene, W. Bloch, et al. 2021. Vertebrate hemicentin-1 interacts physically and genetically with nidogen-2. *bioRxiv*. (Preprint posted November 24, 2021). https://doi.org/10.1101/2021.11.24.469833

Zhang, M., S.H. Chung, C. Fang-Yen, C. Craig, R.A. Kerr, H. Suzuki, A.D.T. Samuel, E. Mazur, and W.R. Schafer. 2008. A self-regulating feed-forward circuit controlling *C. elegans* egg-laying behavior. *Curr. Biol.* 18:1445–1455. https://doi.org/10.1016/j.cub.2008.08.047

Supplemental material

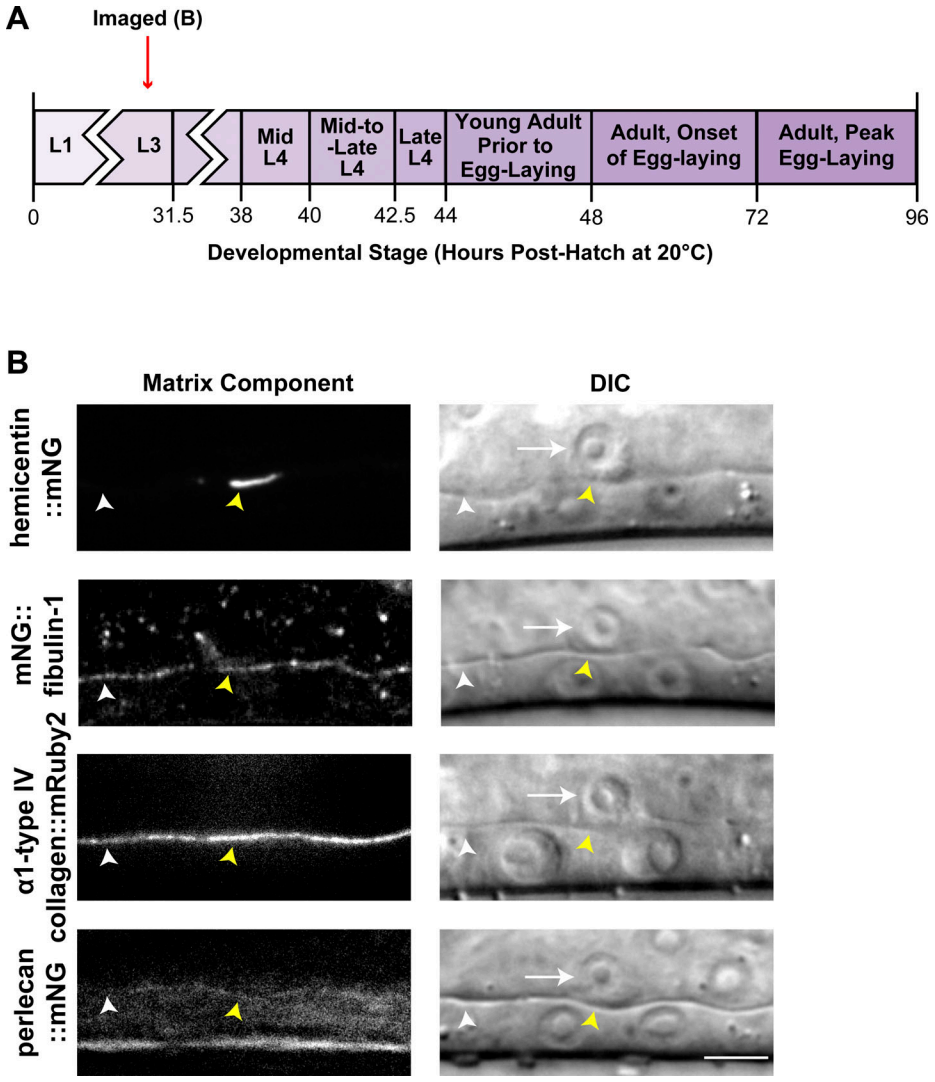

Figure S1. **Utse–seam B-LINK components at the anchor cell B-LINK. (A)** A schematic diagram indicating when imaging was conducted. **(B)** Florescence images (left) and corresponding differential interference contrast (DIC) image (right) of hemicentin::mNG, mNG::fibulin-1, α1-type IV Collagen::mRuby2, and perlecan::mNG underneath the anchor cell (yellow arrowhead) when a B-LINK connects the uterine and epidermal BMs. Hemicentin is enriched underneath the anchor cell (yellow arrowhead) compared to the neighboring BM (white arrowhead), while other matrix components are not enriched. White arrows indicate the anchor cell in DIC images. Scale bar, 5 µm.

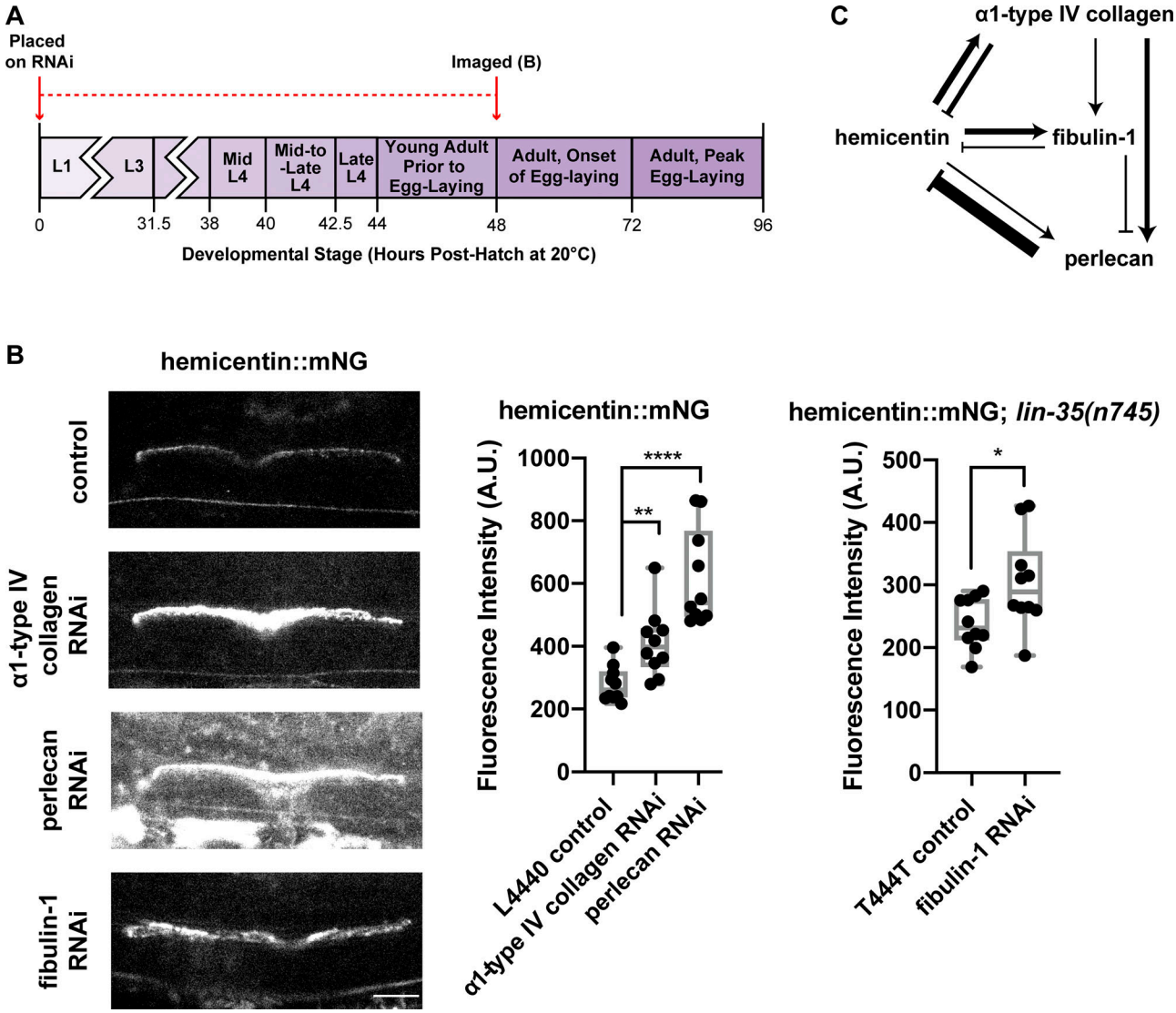

Figure S2. **Dynamic feedback between hemicentin and other B-LINK matrix components. (A)** A schematic figure showing the timing of RNAi treatment and hemicentin::mNG imaging. **(B)** Left: Lateral view fluorescence images of hemicentin::mNG on control (empty vector, *n* = 10), α1-type IV collagen, perlecan, and fibulin-1 RNAi (*n* = 10 each). Right: Mean fluorescence intensity measurements of hemicentin on each RNAi. ****P < 0.0001, **P < 0.01, *P < 0.05, one-way ANOVA followed by post hoc Dunnet's test, unpaired two-tailed Student's *t* test for fibulin-1 RNAi. Box edges in boxplots depict the 25th and 75th percentiles, the line in the box indicates the median value, and whiskers mark the minimum and maximum values. Scale bar, 10 µm. **(C)** A model of matrix interactions that dictate their composition at the utse–seam B-LINK. Also shown in Fig. 7 C.

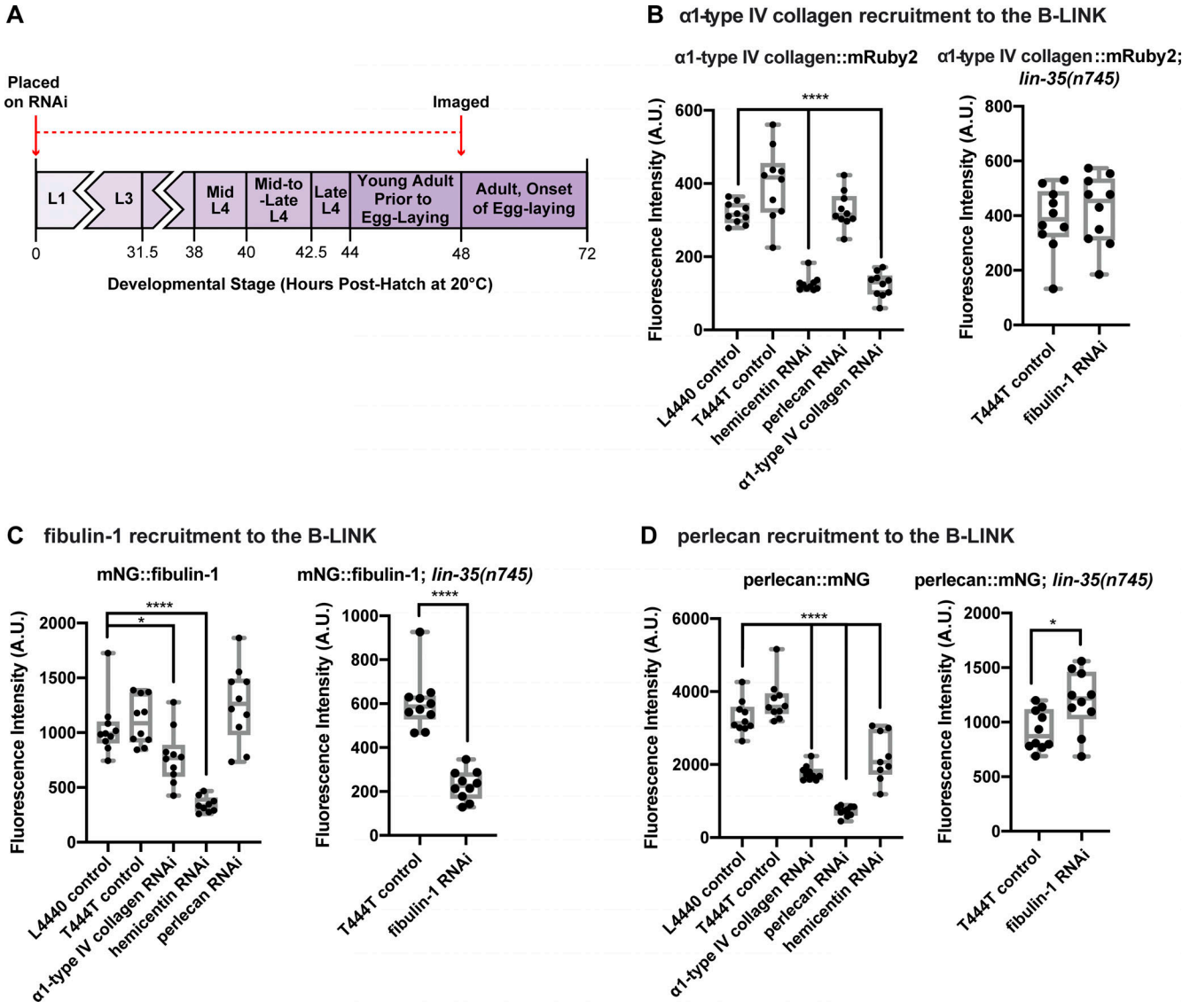

Figure S3. **Dependency of B-LINK matrix components on each other at the B-LINK. (A)** A schematic diagram showing the timing of RNAi knockdown and analysis of utse–seam B-LINK matrix component levels. **(B–D)** Mean fluorescence intensity of B-LINK matrix components α1-type IV collagen::mRuby2, mNG::fibulin-1, and perlecan::mNG on control (L4440/T444T empty vectors) and corresponding B-LINK matrix component RNAi. The role of hemicentin in recruiting other B-LINK matrix components is shown in Figs. 7 and S2. *lin-35*(*n745*) was used for fibulin-1 RNAi to sensitize worms for more efficient knockdown. Box edges in boxplots depict the 25th and 75th percentiles, the line in the box indicates the median value, and whiskers mark the minimum and maximum values. ****P < 0.0001, *P < 0.05, one-way ANOVA followed by post hoc Dunnet's test, unpaired two-tailed *t* test for fibulin-1 RNAi.

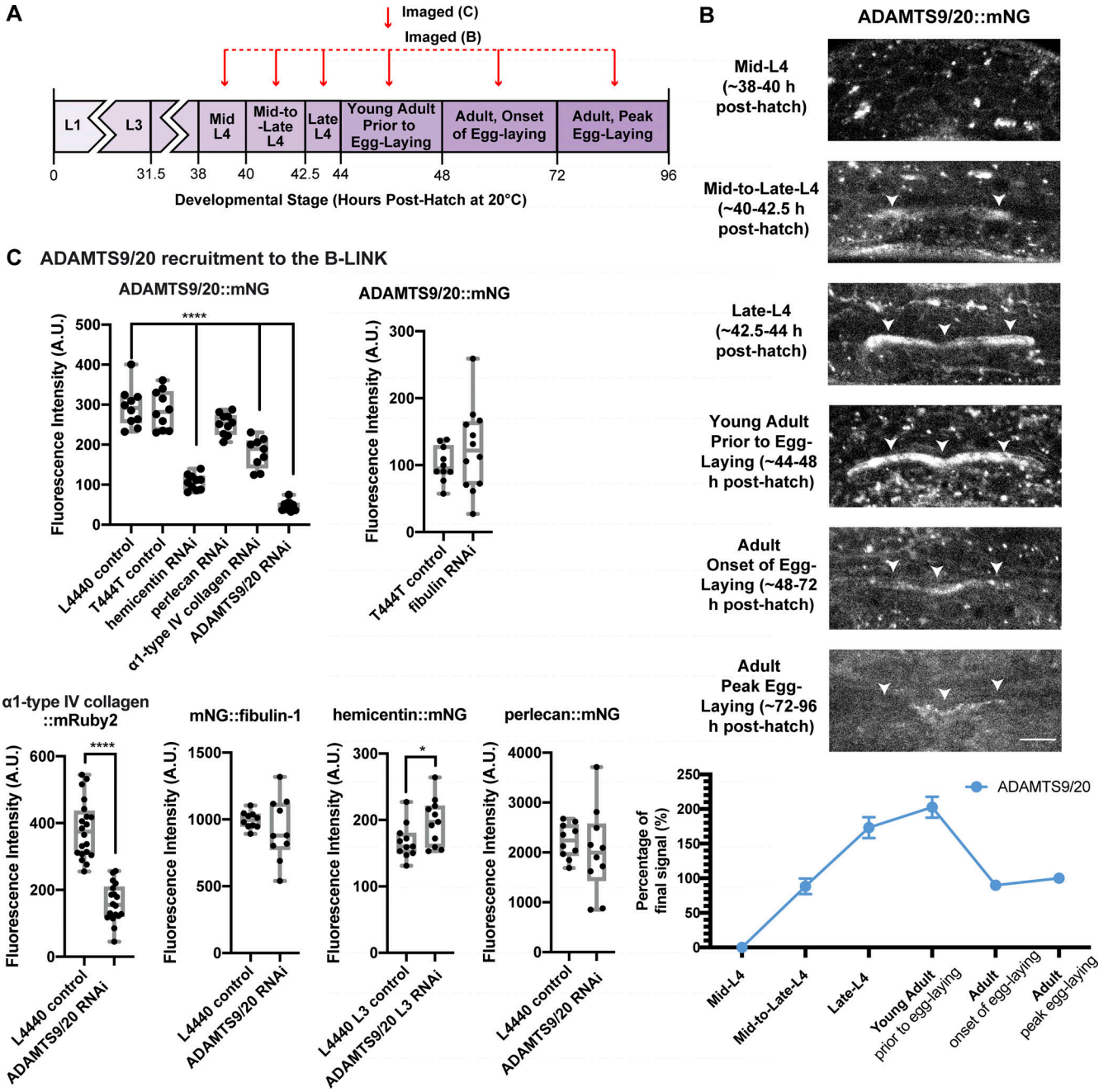

Figure S4. **Characterization of ADAMTS9/20 at the B-LINK. (A)** Schematic timeline showing the timing of imaging. **(B)** Top: Fluorescence images of endogenous ADAMTS9/20::mNG (GON-1) at the B-LINK (white arrowheads) from mid L4 to peak egg-laying in the adult (n = 10 each). Bottom: Quantification of mean florescence intensity of ADAMTS9/20::mNG at each timepoint as a percentage of the final mean fluorescence intensity in the peak egg-laying adult. Error bars represent SEM (n = 10 all stages). Scale bar, 10 µm. **(C)** Mean fluorescence intensity of B-LINK matrix components α1-type IV collagen::mRuby2, mNG::fibulin-1, hemicentin::mNG, perlecan::mNG, and ADAMTS9/20::mNG on control (L4440/T444T empty vectors) and corresponding B-LINK matrix component RNAi. *lin-35*(*n745*) was used for fibulin-1 RNAi to sensitize worms for more efficient knockdown. Box edges in boxplots depict the 25th and 75th percentiles, the line in the box indicates the median value, and whiskers mark the minimum and maximum values. ****P < 0.0001, *P < 0.05, one-way ANOVA followed by post hoc Dunnet's test, unpaired two-tailed t test for fibulin-1 RNAi.

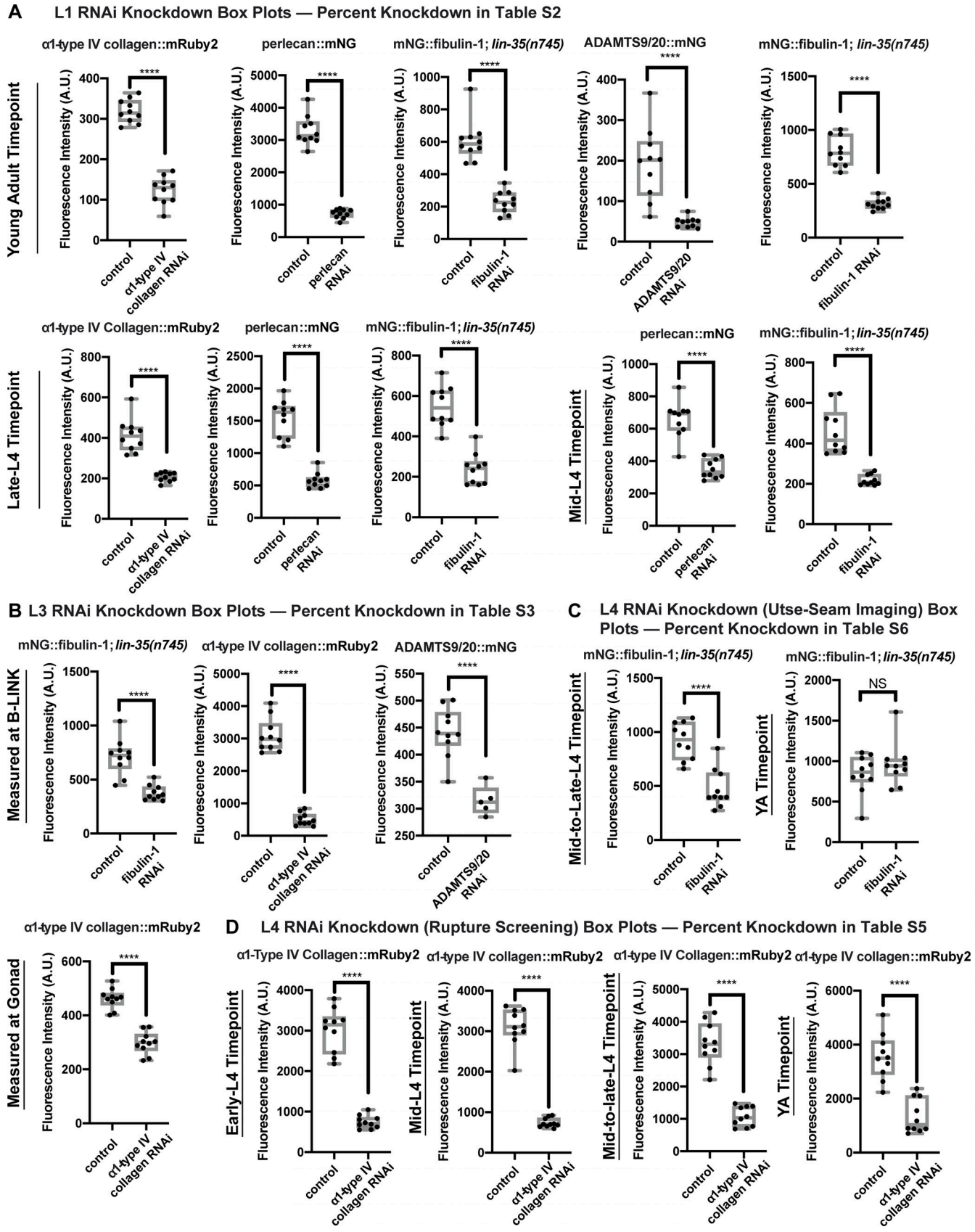

Figure S5. **RNAi Knockdown efficiencies of utse–seam B-LINK matrix components. (A–D)** Quantification of knockdown efficiency for B-LINK matrix component RNAi started at the L1, L3, and L4 stage. ****P < 0.0001, unpaired two-tailed *t* tests. Box edges in boxplots depict the 25th and 75th percentiles, the line in the box indicates the median value, and whiskers mark the minimum and maximum values.

Video 1. **Hemicentin located at the utse–seam B-LINK.** Video shows a 3D reconstruction of hemicentin (visualized with hemicentin::GFP, green) localized at the ends of the utse cell (visualized with *cdh-3p::mCh::moeABD*, red) that contact the seam cells (not shown). The utse marker *cdh-3p::mCh::moeABD* is also expressed in four groups of vulval muscles that extend below the cross-bar of the utse. Related fluorescence images in Fig. 1. Scale bar labeled in video.

Video 2. **Optogenetically induced muscle contraction causes egg-laying.** A transgenic worm expressing the ultraviolet light receptor LITE-1 in body wall and egg-laying muscles (*lite-1*[*ce314*]; *ceIs37* [*myo-3p::lite-1 + myo-3p::GFP*]) grown 60 h on control T444T empty vector RNAi and then exposed to 488 nm light for 7 s to induce extended body wall and egg-laying muscle contractions and forced egg-laying. Stills from video are shown in Fig. 4 B. Video was collected and is displayed at 31.5 frames/s. Scale bar labeled in video.

Video 3. **Optogenetically induced muscle contraction causes uterine rupture after loss of hemicentin.** A transgenic worm expressing the ultraviolet light receptor LITE-1 in body wall and egg-laying muscles (*lite-1*[*ce314*]; *ceIs37* [*myo-3p::lite-1 + myo-3p::GFP*]) grown 60 h on hemicentin RNAi and then exposed to 488-nm light for 7 s to induce body wall and egg-laying muscle contractions. The animal shown undergoes uterine rupture during forced egg-laying. Stills from video are shown in Fig. 4 B. Video was collected and is displayed at 31.5 frames/s. Scale bar labeled in video.

Provided online are eight tables. Table S1 shows rupture screening of basement membrane matrix components. Table S2 shows L1 RNAi knockdown efficiencies. Table S3 shows L3 RNAi knockdown efficiencies. Table S4 shows rupture screening of basement membrane matrix components. Table S5 shows L4 RNAi knockdown efficiencies, rupture experiments. Table S6 shows L4 RNAi knockdown efficiencies, utse–seam imaging. Table S7 shows genes identified that are documented to cause the Rup phenotype. Table S8 shows strain information.